A&A 499, 175–189 (2009)
DOI: 10.1051/0004-6361/200811442


Astronomy & Astrophysics

# Probing the role of protostellar feedback in clustered star formation⋆,⋆⋆

## Mapping outflows in the collapsing protocluster NGC 2264-C

A. J. Maury[1], Ph. André[1], and Z.-Y. Li[2]

[1] Laboratoire AIM, CEA/DSM-CNRS-Université Paris Diderot, IRFU/Service d'Astrophysique, C.E. Saclay, Orme des Merisiers, 91191 Gif-sur-Yvette, France
[2] Department of Astronomy, University of Virginia, PO Box 400325, Charlottesville, VA 22904, USA

Received 28 November 2008 / Accepted 6 February 2009

**ABSTRACT**

*Context.* The role played by protostellar feedback in clustered star formation is still a matter of debate. In particular, protostellar outflows have been proposed as a source of turbulence in cluster-forming clumps, which may provide support against global collapse for several free-fall times.
*Aims.* Here, we seek to test the above hypothesis in the case of the well-documented NGC 2264-C protocluster, by quantifying the amount of turbulence and support injected in the surrounding medium by protostellar outflows.
*Methods.* Using the HERA heterodyne array on the IRAM 30 m telescope, we carried out an extensive mapping of NGC 2264-C in the three molecular line transitions $^{12}$CO(2–1), $^{13}$CO(2–1), and C$^{18}$O(2–1).
*Results.* We found widespread high-velocity $^{12}$CO emission, testifying to the presence of eleven outflow lobes, closely linked to the compact millimeter continuum sources previously detected in the protocluster. We carried out a detailed analysis of the dynamical parameters of these outflows, including a quantitative evaluation of the overall momentum flux injected in the cluster-forming clump. These dynamical parameters were compared to the gravitational and turbulent properties of the clump.
*Conclusions.* We show that the population of protostellar outflows identified in NGC 2264-C is likely to contribute a significant fraction of the observed turbulence but cannot efficiently support the protocluster against global collapse. Gravity appears to largely dominate the dynamics of the NGC 2264-C clump at the present time; however it is possible that an increase in the star formation rate during the later evolution of the protocluster will trigger enough outflows to finally halt the contraction of the cloud.

**Key words.** stars: formation – stars: circumstellar matter – ISM: clouds – ISM: structure – ISM: jets and outflows – ISM : individual objects: NGC 2264-C

## 1. Introduction

### 1.1. Clustered star formation, turbulence and protostellar feedback

It is now well established that a large fraction of young stars in giant molecular clouds form in groups and clusters rather than in isolation (e.g. Carpenter 2000; Adams & Myers 2001; Lada & Lada 2003).

Three main classes of models have been proposed for regulating the star formation process and explaining the origin of the stellar initial mass function (IMF) in young star clusters. The first scenario is based on turbulent fragmentation of the parent molecular cloud (e.g. Padoan & Nordlund 2002; Hennebelle & Chabrier 2008), which produces an IMF-like core mass distribution as observed in the nearest cluster-forming regions (e.g. Motte et al. 1998; Stanke et al. 2006). Briefly, self-gravitating pre-stellar condensations (each containing one local Jeans mass) form as turbulence-generated density fluctuations, then decouple from their turbulent environment, and eventually collapse with little interaction with their surroundings. In this picture, the IMF results primarily from the properties (e.g. power spectrum) of *interstellar* turbulence, which also controls the global star formation rate and efficiency (e.g. Mac Low & Klessen 2004; Krumholz & Tan 2007). The second class of models emphasizes the role of *protostellar* turbulence and feedback in regulating the star formation process (e.g. Norman & Silk 1980; Adams & Fatuzzo 1996; Shu et al. 2004). Here, the IMF and the star formation efficiency are determined by the stars themselves through the collective effects of their feedback on both individual cores and the parent cloud. A third scenario exists, however, according to which turbulence is only responsible for forming protostellar seeds but plays no direct role in regulating the star formation process and shaping the IMF, which is mainly determined by competitive accretion and dynamical interactions between individual cluster members (e.g. Bonnell et al. 2001; Bate et al. 2003).

From an observational perspective, millimeter-wave observations of molecular clouds have revealed supersonic linewidths, which are presumably due to turbulent motions. Theory suggests that turbulent motions can be treated as an additional pressure (e.g. Chandrasekhar 1951; Von Weizsäcker 1951), so that supersonic turbulence increases the effective Jeans mass supported against collapse.

⋆ Based on observations carried out with the IRAM 30 m telescope. IRAM is supported by INSU/CNRS (France), MPG (Germany), and IGN (Spain).
⋆⋆ The Fits files for the CO(2–1) HERA maps are only available in electronic from at the CDS via anonymous ftp to cdsarc.u-strasbg.fr (130.79.128.5) or via http://cdsweb.u-strasbg.fr/cgi-bin/qcat?J/A+A/499/175

Protostellar outflows have long been considered a plausible way of driving a significant fraction of molecular cloud turbulence, especially in cluster-forming clumps, where stars form more efficiently than in the bulk of molecular gas (Bally et al. 1996; Reipurth & Bally 2001; Knee & Sandell 2000). Recently, Nakamura & Li (2007) discussed the possible effects of protostellar outflows on cluster formation. In particular, they argued that, due to its short decay time (e.g. Mac Low et al. 1998), the "interstellar turbulence" initially present in a cluster-forming clump is quickly replaced by turbulent motions generated by protostellar outflows. According to Nakamura & Li, the protostellar outflow-driven turbulence dominates for most of a protocluster's lifetime and acts to maintain the cluster-forming region close to overall virial equilibrium for several dynamical times, avoiding global free-fall collapse. The exact mechanism by which outflows inject turbulence in the parent cloud is not well understood yet and may involved fossil cavities (e.g. Quillen et al. 2005; Cunningham et al. 2006). On the scale of an entire giant molecular cloud, the shocks produced by outflows from young stars may not inject momentum and energy at a high enough rate to counter the rate at which turbulent energy decays (see Banerjee et al. 2007). On the other hand, intense outflow activity within a young protocluster may be sufficient to support the parsec-scale parent gas clump, thereby modifying the outcome of the star formation process.

As the role of protostellar feedback in cluster-forming clouds is still a matter of debate, detailed studies of the dynamical effects of protostellar outflows in young protoclusters, where outflows are particularly strong and numerous, are required to fully understand the process of clustered star formation. In this paper, we test some of the above ideas by quantifying the impact of protostellar outflows on the dynamics of the NGC 2264-C clump, a protocluster at a very early stage of evolution.

### 1.2. Our target region: NGC2264-C

The NGC 2264 cluster-forming region is located in the Mon OB1 giant molecular cloud complex at a distance $d \sim 800$ pc. The cloud associated with NGC 2264 has been the target of several millimeter line studies, including an unbiased CO ($J = 1 \rightarrow 0$) survey for molecular outflows (Margulis et al. 1988) and a search for dense gas via multitransitional CS observations (Wolf-Chase et al. 1995; Wolf-Chase & Walker 1995). These early studies revealed two prominent molecular clumps, named NGC 2264-C and NGC 2264-D, each associated with a CO outflow. The NGC 2264 region also harbors a young star cluster of more than 360 near-IR sources (Lada et al. 1993; Lada & Lada 2003). The most luminous object of the cluster, hereafter called IRS1 after Allen (1972), is embedded in NGC 2264-C and associated with the Class I IRAS source IRAS 06384+0932 ($L_{\rm bol} \sim 2300\ L_\odot$ – Margulis et al. 1989).

The internal structure of NGC 2264-C and NGC 2264-D was subsequently resolved by higher-resolution millimeter and submillimeter studies (Ward-Thompson et al. 2000; Williams & Garland 2002; Peretto et al. 2006, 2007). In particular, through 1.2 mm continuum observations, Peretto et al. (2006) identified 12 compact dense cores in NGC 2264-C (see Fig. 1), of which at least 8 are Class 0-like objects with associated near-IR $H_2$ jets (Wang et al. 2002) or compact CS outflows (Schreyer et al. 2003). These cores have typical diameters ~0.04 pc, masses ranging from ~2 to ~40 $M_\odot$, and column densities ranging from $\sim 4 \times 10^{22}$ to $\sim 6 \times 10^{23}$ cm$^{-2}$. Based on $HCO^+$, CS, and $N_2H^+$ mapping observations, Peretto et al. (2006) also showed the presence of large-scale collapse motions converging onto the most massive core (C-MM3 with $M \sim 40\ M_\odot$), near the center of NGC 2264-C. The IRAM Plateau de Bure interferometer observations of Peretto et al. (2007) revealed a thirteenth source, C-MM13, located only 13.5″ (or ~0.05 pc) away from C-MM3.

In their study, Peretto et al. (2007) successfully modeled the dynamical evolution of the NGC 2264-C protocluster. They compared the available millimeter observations with SPH numerical simulations of the collapse of a Jeans-unstable, prolate

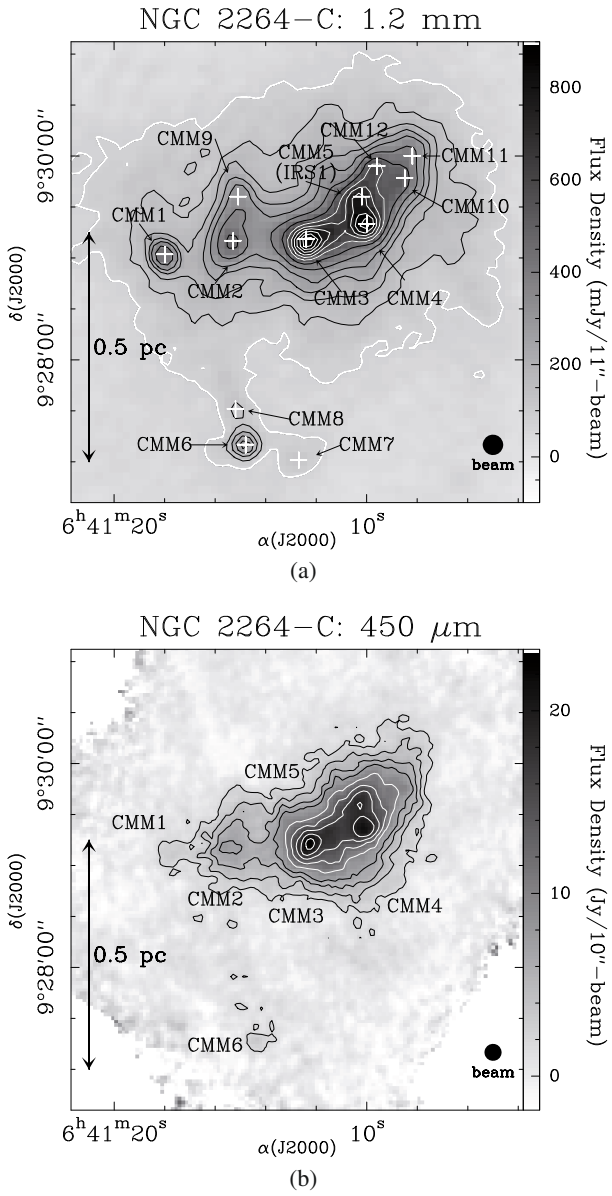


**Fig. 1. a)** Dust continuum map of NGC 2264-C taken at 1.2 mm by Peretto et al. (2006) with the MAMBO bolometer array on the IRAM 30 m telescope. Twelve millimeter peaks were found and interpreted as candidate Class 0 objects (see Peretto et al. for details). **b)** Total-power 450 $\mu$m dust continuum map of the NGC 2264-C protocluster taken by us with the P-ArTéMiS bolometer camera[1] on the APEX telescope. The HPBW resolution is ~10″. The contour levels go from 1.75 to 7 Jy/10″-beam by 1.75 Jy/10″-beam and from 10 to 22 Jy/10″-beam by 3 Jy/10″-beam.

[1] P-ArTéMiS is a 16 × 16-pixel prototype of the large-format submillimeter bolometer camera currently being built by CEA for the APEX telescope (cf. André et al. 2008; Talvard et al. 2008). http://www.apex-telescope.org/instruments/pi/artemis/

dense clump. Peretto et al. (2007) obtained a good quantitative agreement with observations when starting from a low level of initial turbulent energy. However, the total mass of dense gas (i.e., with $n_{H_2} > 10^4\,cm^{-3}$) was ~10 times lower in the best-fit simulations than in the actual NGC 2264-C clump. When Peretto et al. (2007) increased the mass of dense gas by a factor of 10 in their numerical simulations, a larger number of cores was generated, leading to a poor match to the observations. It seemed therefore that an additional source of support against gravity, not included in the simulations of Peretto et al. (2007), had to be invoked to explain the current dynamical state NGC 2264-C. Peretto et al. suggested that this extra support could arise from protostellar feedback and/or magnetic fields.

Because it is well documented and known to exhibit outflow activity (Margulis et al. 1988), the NGC 2264-C protocluster is an ideal laboratory for probing the initial conditions of clustered star formation and evaluating the impact of outflow feedback on early protocluster evolution. We thus initiated a mapping study of the outflow already detected by Margulis et al. (1988) in NGC 2264-C, with higher angular resolution and better sensitivity. Our goal was to assess the momentum injection rate due to outflows in this protocluster and examine whether outflows could affect the global dynamical evolution of the protocluster.

## 2. Observations and data reduction

### 2.1. Observations

Observations of the $^{12}$CO(2–1), C$^{18}$O(2–1) and $^{13}$CO(2–1) emission lines (see Table 1) from the NGC 2264-C protocluster were taken with the IRAM-30 m telescope between October and November 2006 using the HEterodyne Receiver Array HERA (Schuster et al. 2004) together with the VESPA autocorrelator backend. HERA is an assembly of two focal plane arrays (HERA1 and HERA2) of 9 SIS receivers each. The two arrays have orthogonal polarization and their 9 pixels are arranged in the form of a center-filled square and are separated by 24″. HERA1 and HERA2 were used simultaneously, allowing us to map the same region of the sky at two different frequencies at the same time. VESPA was used with a channel spacing of 320 kHz for $^{12}$CO(2–1), and 80kHz for C$^{18}$O(2–1) and $^{13}$CO(2–1). The VESPA autocorrelator configurations used during our observations can be found in Table 1. Observations were carried out in position switched On-The-Fly (OTF) mode, scanning NGC 2264-C in right ascension and declination. We adopted a drift speed of 2″/s with a dump time of 2 s, and HERA was rotated by 9.5 ° to obtain a spacing of 4″ between adjacent scan lines, while a derotator was used to keep the HERA pixel pattern stationary in the Nasmyth focal plane. All this resulted in a sampling of 4″ over the entire map. The half power beamwidth (HPBW) of the 30-m telescope being of 11″ at this frequency, this corresponds to an over-Nyquist sampling. The resulting map has a size of 3.3′ × 3.3′ (equivalent to ~0.8 pc$^2$ at the distance of the protocluster). The emission-free reference position was located at offsets (−1500″, −1500″) from the protostellar core C-MM3, located at the center of our map. The typical system temperatures varied between ~300 K and ~600 K. The telescope pointing was checked every ~2 h on J0528+134, while focus checks and adjustments were made every ~3 h on the strong source NGC 7538. The observations were carried out in single sideband mode with an image rejection of ~10 dB, providing a calibration accuracy better than ~10%. At 230 GHz, the main beam efficiency and the forward efficiency of the telescope are $B_{\rm eff} = 0.90$ and $F_{\rm eff} = 0.52$ respectively. Throughout this paper, the line intensity scale adopted is in units of $T_{\rm A}^*$, the equivalent antenna temperature above the atmosphere.

**Table 1.** Parameters of the IRAM 30 m observations.

| Line | Frequency (GHz) | Resolution (km s$^{-1}$) | Bandwidth (km s$^{-1}$) | Mean rms noise[a] (K) |
|---|---|---|---|---|
| $^{12}$CO(2–1) | 230.5379 | 0.84 | 157 | 0.1 |
| $^{13}$CO(2–1) | 220.3986 | 0.10 | 78 | 0.2 |
| C$^{18}$O(2–1) | 219.5603 | 0.10 | 78 | 0.3 |

[a] rms noise per spectral resolution element.

We also mapped the NGC 2264-C region in the 450 $\mu$m dust continuum at ~10″ resolution (HPBW) with the P-ArTéMiS bolometer array on the Atacama Pathfinder Experiment (APEX) telescope in November 2007. The resulting map is shown in Fig. 1b, and details about the P-ArTéMiS camera and the November 2007 run at APEX can be found in André et al. (2008).

### 2.2. Data reduction

All data were reduced with the CLASS90 program, a new part of the GILDAS software package. Dedicated CLASS90 scripts were written to automatically reduce the data and produce a datacube for each of the three observed transitions (see Table 1).

Linear (first-order) baselines were determined from velocity ranges where emission is no longer positively detected above the 3$\sigma$ noise limit anywhere in the map, and then subtracted from the spectra. We stress that our HERA observations resulted in very good baselines (see example in Fig. 4). We used 5 km s$^{-1}$-wide velocity windows at either end of the $^{12}$CO(2–1) spectra to fit the substracted baselines, making us sensitive to any outflow emission present up to LSR velocities of $V_{\rm sys} \pm 55$ km s$^{-1}$.

Some velocity channels showed spikes due to band splitting of the VESPA autocorrelator. We had to flag them and replace their values by interpolating the closest two good channels. The worst case occurred around $v_{\rm LSR} \sim +23$ km s$^{-1}$ with four consecutive bad channels, leading to an interpolation over ~1.7 km s$^{-1}$, which we consider as being negligible for the present study of high-velocity emission.

Finally, in order to improve the signal-to-noise ratio, we also smoothed the initial velocity resolution by a factor of two for the $^{12}$CO(2–1) map, leading to a final spectral resolution of 0.84 km s$^{-1}$ per channel.

## 3. Mapping results and analysis

We detected a total of eleven sub-regions or "lobes" exhibiting high-velocity emission in the $^{12}$CO(2–1) map (Fig. 2). These eleven lobes are spatially distributed around the millimeter continuum cores identified by Peretto et al. (2006, 2007), and four of these lobes can be directly associated with Class 0 – like objects, as discussed in Sect. 5.1 below.

In Sect. 3.1 we explore the kinematical properties of these eleven outflow lobes, while Sect. 3.2 discusses the optical depth of the $^{12}$CO(2–1) transition in our map.

### 3.1. Spatial extent of the outflow lobes and minimum associated velocity intervals

In order to determine the spatial extent of each outflow, we need to find out which pixels exhibit high-velocity emission due to

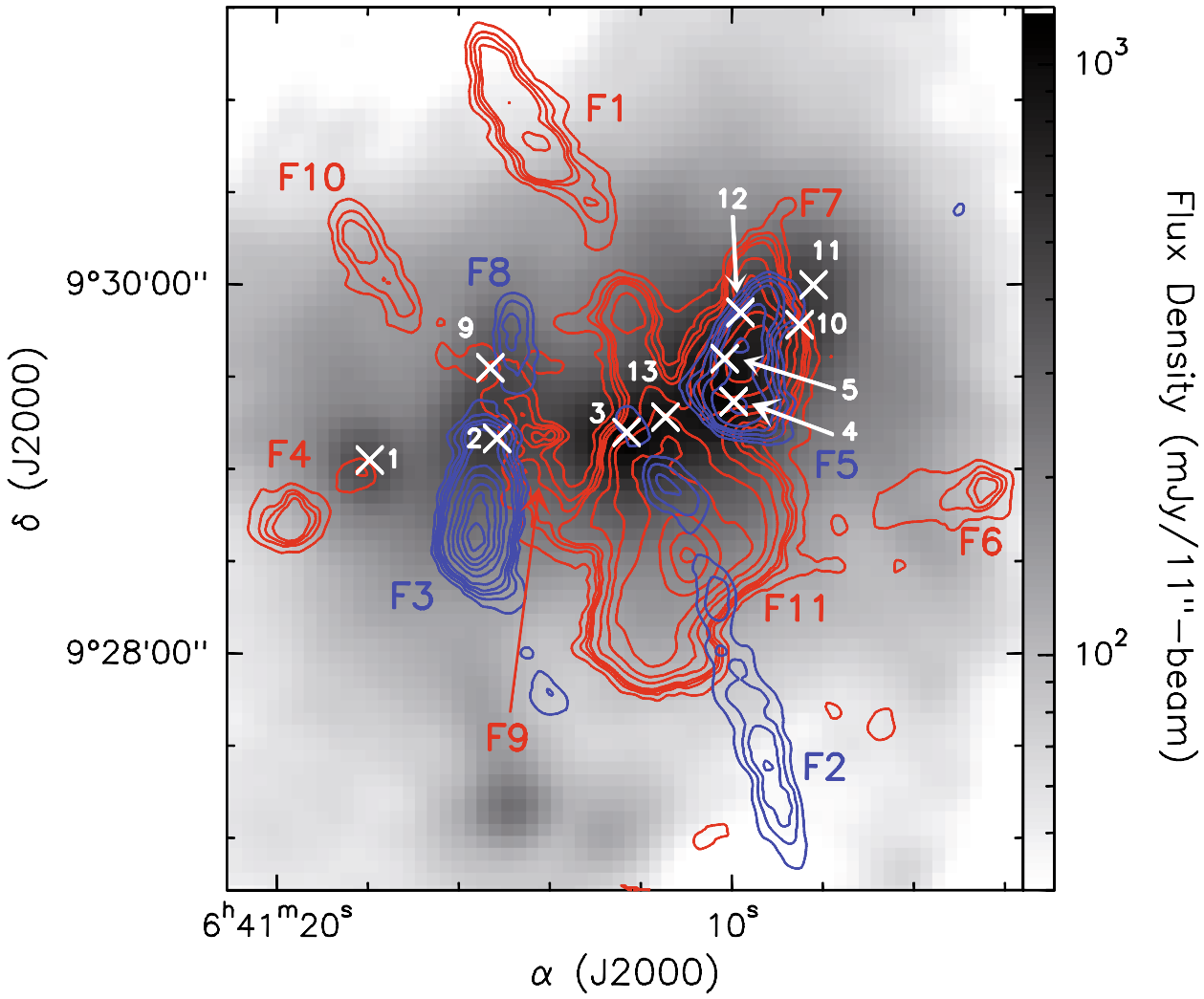


**Fig. 2.** $^{12}$CO(2–1) map of the NGC 2264-C protocluster. Blue contours show the levels of $^{12}$CO(2–1) intensity integrated between −27 km s$^{-1}$ and 2 km s$^{-1}$ in the blue-shifted part of the line, and go from 5 to 98 K km s$^{-1}$. Red contours are levels of intensity integrated between 13 km s$^{-1}$ and 34 km s$^{-1}$ in the red-shifted part of the line, and go from 5 to 110 K km s$^{-1}$. The eleven outflows discovered in the present survey are labeled by F1 to F11. The background greyscale image is the 1.2 mm dust continuum map obtained by Peretto et al. (2006) with MAMBO on the IRAM-30 m. White crosses and numbers refer to the millimeter continuum peaks identified by Peretto et al. (2006, 2007) (see also Fig. 1).

outflows. We know from previous work that the NGC 2264-C protocluster exhibits a complex pattern of cloud velocities: the mean LSR velocity of the cloud was found to be 7.5 ± 0.2 km s$^{-1}$, but a pronounced velocity discontinuity was also found by Peretto et al. (2006) near CMM3, and local systemic velocities can depart from this value by up to 0.7 km s$^{-1}$, depending on position in the protocluster. Likewise, the intrinsic $^{12}$CO(2–1) linewidth varies with position as column density and turbulent motions vary through the protocluster. Therefore, to discriminate emission due to high-velocity outflow motions from emission due to an intrinsically wider $^{12}$CO(2–1) line from the cloud itself, and thus identify those pixels with outflow emission, we adopted the following conservative method.

We first constructed $^{12}$CO(2–1) reference spectra for the local ambient medium surrounding the high-velocity lobes. In practice, we constructed each reference spectrum by averaging a large number of spectra (from 30 to 200 spectra depending on the subregion considered) located in the close neighborhood of each candidate outflow. In this way, we obtained one reference spectrum per high-velocity lobe for outflows F3 to F11. We constructed two reference spectra for each of F1 and F2, so as to ensure that small variations in the systemic velocity occurring between different sub-regions of these extended lobes be properly accounted for. In a second step, we compared each reference spectrum with the corresponding high-velocity lobe line profiles. Each pixel which showed emission stronger than three times the typical noise level, $\sigma_{\rm spec}$, in the $^{12}$CO(2–1) outflow spectrum in three consecutive channels (corresponding to a 2.5 km s$^{-1}$-wide window in velocity), at velocities where emission was no longer detected in the reference spectrum, was assigned to the candidate outflow under consideration.

Such cases are illustrated in Fig. 3, using spectra from the two outflows F8 and F9, for which obvious high-velocity wings are observed, at blueshifted and redshifted velocities, respectively. The vertical solid lines mark the velocity range over which emission is only due to outflow material: in this velocity range no emission is detected in the reference spectrum, while emission is positively detected in the spectra from the candidate outflow. Here, we ignore any additional outflow emission at lower velocities where emission is still seen in the reference spectrum. Distinguishing between low-velocity outflow emission and turbulent broadening of the line spectrum from the

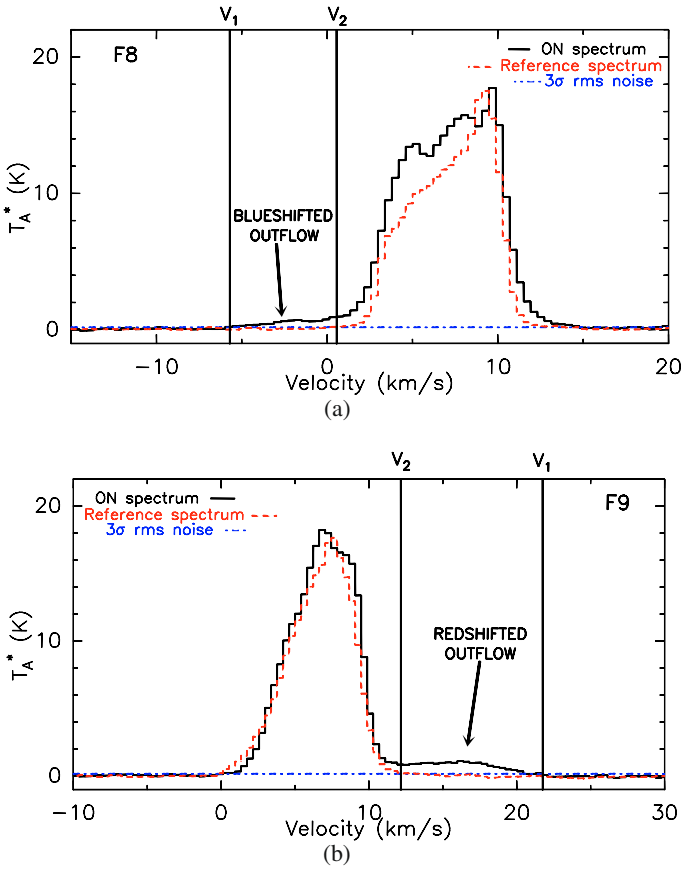


**Fig. 3.** Examples of high-velocity $^{12}$CO(2–1) spectra showing emission at blue-shifted **a)** and red-shifted **b)** velocities for the candidate outflows F8 and F9, respectively. In both cases, the dashed spectrum shows a $^{12}$CO(2–1) reference spectrum obtained by averaging ∼100 spectra from the ambient cloud emission in the immediate vicinity of the outflow. Vertical solid lines highlight the velocity range over which emission is no longer detected from the ambient cloud, whereas blue-shifted or red-shifted high-velocity emission is still present in the spectrum (above the $3\sigma$ noise level shown as an horizontal dot-dashed line).

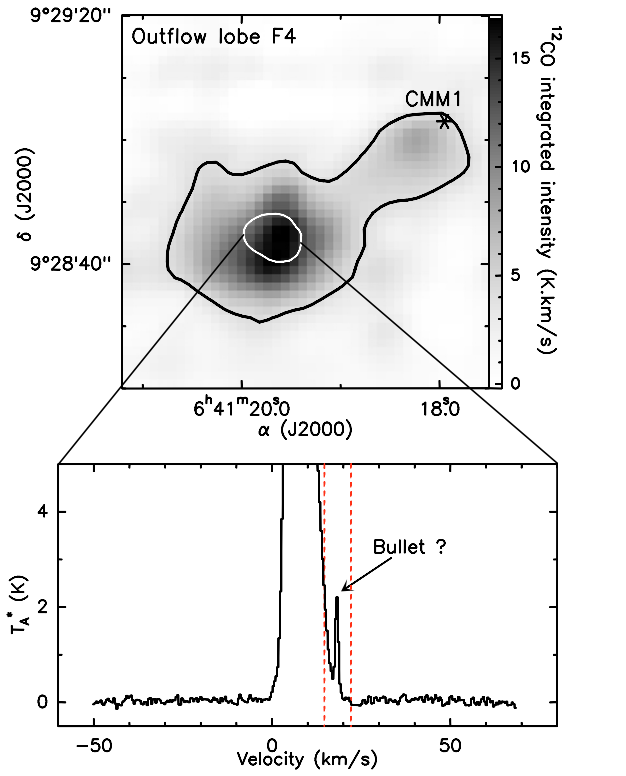


**Fig. 4.** Spatial extent of the red-shifted outflow lobe F4. *The upper panel* shows the high-velocity $^{12}$CO(2–1) emission, integrated from +14.3 km s$^{-1}$ to +23 km s$^{-1}$ (velocity interval marked by dashed lines in *the lower panel*). In this case, the *reference* spectrum associated to F4 does not show any significant emission at LSR velocities greater than 14.3 km s$^{-1}$. The $3\sigma_{\rm spec}$ level mentioned in the text corresponds to the thick black contour. All pixels showing integrated emission above this value were therefore assigned to outflow F4. A typical $^{12}$CO(2–1) spectrum observed near the peak of outflow emission is shown in the lower panel. Note the quality of the baseline and the detached high-velocity feature at $v_{\rm LSR} \sim +18$ km s$^{-1}$. The area over which such a "bullet-like" emission feature (see Sect. 5.1) is seen in F4 is marked by the white contour in the upper panel.

ambient cloud is more uncertain. We will try to account for the low-velocity outflow emission when we estimate outflow parameters in Sect. 4 below. For the purpose of determining the spatial extents of the outflows, however, only those pixels satisfying the selection criteria described above were included.

Following this procedure for all pixels in the map, we were able to determine the spatial extent of each outflow lobe (see Col. 4 of Table 2 for the values, and Fig. 4 for an example). The velocity range over which high-velocity emission was detected from the outflow lobe but no emission was seen in the reference spectrum will be adopted as the main LSR velocities interval to be considered in further calculations. In the following, $|V_1|$ will denote the extreme LSR velocity observed toward the outflow (beyond which $T_{\rm outflow} < 3\sigma_{\rm spec}$), and $|V_2|$ will denote the minimum LSR velocity at which unambiguous outflow emission is detected (beyond which $T_{\rm ref} < 3\sigma_{\rm spec}$ while $T_{\rm outflow} > 3\sigma_{\rm spec}$). As can be seen in Table 2, the velocity ranges spanned by the observed high velocity emission vary from outflow to outflow, and $^{12}$CO(2–1) emission is detected at very high LSR velocities in some cases (up to −27 km s$^{-1}$ in the case of the blue-shifted lobe F2).

### 3.2. Optical depth of the $^{12}$CO(2–1) emission

In order to derive the masses and moments for the eleven candidate outflows, we need to assess the optical depth of the CO emission. We used our observations in three isotopes (see Table 1) to estimate the optical depth of the CO(2–1) transition in our data.

We first used our C$^{18}$O(2–1) data to check that the $^{13}$CO(2–1) emission observed away from line center was optically thin over the entire mapped area and estimated a maximum optical depth $\tau\left(^{13}\mathrm{CO}\right) \sim 0.75$ at the systemic velocity of the ambient cloud.

We then derived the $^{12}$CO(2–1) optical depth in the high-velocity gas from the observed $^{12}$CO/$^{13}$CO line intensity ratio (cf. Goldsmith et al. 1984). We measured this ratio at eleven positions, chosen to coincide with the positions of the candidate outflows in the $^{12}$CO map. Assuming that the excitation temperatures of the $^{12}$CO and $^{13}$CO lines are equal, and knowing that the $^{13}$CO emission is optically thin, the $^{12}$CO optical depth $^{12}\tau(v)$ at any given velocity $v$ is related to the $^{12}$CO/$^{13}$CO intensity ratio by:

$$\frac{I\left(^{12}\mathrm{CO}\right)_v}{I\left(^{13}\mathrm{CO}\right)_v} = \frac{1-\exp^{-^{12}\tau(v)}}{^{13}\tau(v)} = \frac{1-\exp^{-^{12}\tau(v)}}{^{12}\tau(v)} \cdot X_{\rm iso}, \quad (1)$$

**Table 2.** Observed properties of the $^{12}$CO(2–1) outflows detected in the map of Fig. 2.

| OUTFLOW LOBE | Local systemic [(1)] velocity $V_{sys}$ (km s$^{-1}$) | Outflow main [(2)] LSR velocities interval (km s$^{-1}$) | | Area [(3)] (arcsec$^2$) | Length [(4)] (arcsec) |
|---|---|---|---|---|---|
| | | $V_1$ | $V_2$ | | |
| F1 (Red) | 7.5 | 28.5 | 13 | 2780 | 127 |
| F2 (Blue) | 7.6 | −27 | 1.1 | 3060 | 184 |
| F3 (Blue) | 7.4 | −26.6 | 1.4 | 1935 | 70 |
| F4 (Red) | 7.7 | 23 | 14.3 | 900 | 53 |
| F5 (Blue) | 7.3 | −12 | 0.3 | 1080 | 50 |
| F6 (Red) | 7.1 | 28.1 | 13.1 | 1360 | 56 |
| F7 (Red) | 7.2 | 33.2 | 14.7 | 2230 | 72 |
| F8 (Blue) | 7.2 | −23 | 1.7 | 590 | 38 |
| F9 (Red) | 7.2 | 30.2 | 13.7 | 800 | 53 |
| F10 (Red) | 7.2 | 32.2 | 13.7 | 610 | 50 |
| F11 (Red) | 7.7 | 33 | 15.2 | 4180 | 90 |

(1) Systemic LSR velocity of the ambient material around each outflow.
(2) Velocity interval [$V_1$; $V_2$] over which each outflow emission is detected but no significant emission is seen in the reference spectrum.
(3) Surface area of each outflow lobe.
(4) Major size of each outflow lobe.

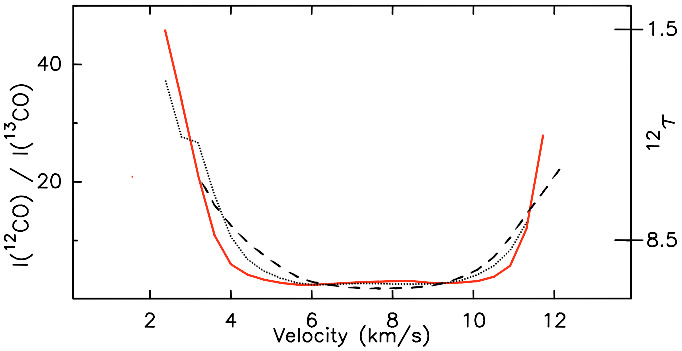


**Fig. 5.** $^{12}$CO(2–1) to $^{13}$CO(2–1) intensity ratio calculated over the widest velocity range for which the $^{13}$CO(2–1) intensity is greater than the 3$\sigma$ noise limit. Outflow F4 is represented as a solid line, outflow F7 as a dashed line, and outflow F3 as a dotted line. The vertical axis on the right shows the corresponding values of the $^{12}$CO(2–1) optical depth, $^{12}\tau(v)$.

where $X_{iso}$ is the [$^{12}$CO]/[$^{13}$CO] abundance ratio, here assumed to have the terrestrial value of 89 (Wilson & Matteucci 1992). The signal-to-noise ratio in the $^{13}$CO(2–1) spectra was not adequate to derive $^{12}\tau_v$ over the full velocity extent of the line wings seen in $^{12}$CO(2–1). We calculated the isotopic ratio up to velocities where the $^{13}$CO(2–1) emission became lower than the 3$\sigma$ noise limit, on either side of the line centroid for the eleven outflows. Figure 5 shows the $^{12}$CO(2–1) to $^{13}$CO(2–1) ratio for three different outflows (outflow F4 as a solid line, outflow F7 as a dashed line, and outflow F3 as a dotted line).

The $^{12}$CO(2–1)/$^{13}$CO(2–1) intensity ratio is expected to increase, and $^{12}\tau_v$ to decrease, at greater velocity offsets from the line centroid, but the $^{13}$CO(2–1) emission becomes undetectable at these high velocities. At the highest velocities showing detectable $^{13}$CO(2–1) emission, a maximum $^{12}$CO(2–1)/$^{13}$CO(2–1) intensity ratio of ∼45 is measured for both blueshifted and redshifted gas (cf. Fig. 5), which corresponds to $^{12}\tau_{wings} \sim 1.5$. Therefore, $^{12}\tau$ is much lower than 1.5 at LSR velocities greater than 12 km s$^{-1}$ or lower than 2 km s$^{-1}$. As the velocity intervals derived in Sect. 3.1.2 for the candidate outflows lie outside the [2:12] km s$^{-1}$ range, we conclude that the $^{12}$CO(2–1) outflow emission is optically thin at both blue-shifted and red-shifted velocities.

Note, however, that we will apply an optical depth correction factor when we derive the amount of mass entrained by the outflows at low velocities (i.e., inside the [2:12] km s$^{-1}$ range) in Sect. 4.1.2 below. For this purpose, we will use the values of $^{12}\tau(v)$ estimated at LSR velocities between +2 and +12 km s$^{-1}$ (see Fig. 5 for examples).

## 4. Momentum injection rate due to outflows in NGC 2264-C

Our $^{12}$CO(2–1) map revealed the presence of eleven outflows in the NGC 2264-C protocluster. To quantify the effective feedback that these eleven outflows produce on the protocluster, we now estimate the masses of outflow entrained material, as well as the outflow dynamical parameters.

### 4.1. Outflow mass estimates

#### 4.1.1. Method of derivation

Assuming local thermal equilibrium (LTE), the total gas mass of an outflow can be obtained from the observed $^{12}$CO(2–1) spectra as follows (see, e.g., Scoville et al. 1986):

$$M_{\rm flow} = 5.3\times10^{-8}\times\frac{T_{\rm ex}+0.93}{e^{\frac{-16.77}{T_{\rm ex}}}}\times d^2\times\int_{V_a}^{V_b}\int_A I(v)\,{\rm d}v{\rm d}A\ (M_\odot), \quad (2)$$

where $T_{ex}$ is the CO excitation temperature (in Kelvin), and $d$ the distance to the source expressed in kpc. $I(v)$ is related to the observed antenna temperature $T_A^*(v)$ (expressed in Kelvin) by $I(v) = \left(\frac{\tau_v}{1-e^{-\tau_v}}\right)\times T_A^*(v)$, and $\int_{V_a}^{V_b}\int_A I(v)\,{\rm d}v{\rm d}A$ (with $I(v)$ in K, d$v$ in km s$^{-1}$, and d$A$ in arcsec $^2$) is the $^{12}$CO(2–1) intensity integrated over the surface area $A$, and over the velocity interval [$V_a$:$V_b$] of the outflow. In deriving this formula, we adopted a standard CO to $H_2$ abundance ratio, $[\frac{CO}{H_2}] = 10^{-4}$ (Frerking et al. 1982).

#### 4.1.2. Masses of outflow-entrained gas

We first computed the *minimum* mass of gas associated with each outflow, assuming that the whole outflow emission is included in the main LSR velocity range $[V_1{:}V_2]$ derived in Sect. 3.1.2 (Col. 3 of Table 2). In this first estimate, we thus did not take into account any additional outflow emission seen at lower absolute velocity offsets from line center, where emission is positively detected in the reference spectrum (see Fig. 6). We showed in Sect. 3.2 that the $^{12}$CO(2–1) emission is optically thin everywhere outside the velocity range [2:12] km s$^{-1}$ in our map. As the minimum velocity intervals considered in this first estimate all lie outside the [2:12] km s$^{-1}$ range, the minimum masses of outflowing gas can thus be computed as:

$$M_{\rm min} = 1.6 \times 10^{-6} \times \int_{V_1}^{V_2} \int_A T_{\rm A}^*(v)\, {\rm d}v\, {\rm d}A\ (M_\odot). \quad (3)$$

In the above equation, $T_{\rm A}^*(v)$ is expressed in Kelvin, d$v$ is a velocity bin (in km s$^{-1}$), while d$A$ corresponds to the surface element (in arcsec$^2$).

The main source of uncertainty on the derived outflow-entrained masses is the uncertain value of the CO excitation temperature. For optically thin CO emission, the excitation temperature is expected to be close to the gas kinetic temperature due to the low dipole moment of the CO molecule. Nevertheless, large temperatures (up to 80 K), due to gas heating by outflow shocks (Umemoto et al. 1992; Bachiller et al. 1993, 2001) are sometimes found in CO outflows. As can be seen from Eq. (2), the derived outflow mass is almost proportional to the assumed excitation temperature. We assumed an excitation temperature of 20 K in our calculations, which is representative of typical CO ouflows. The uncertainty in the CO excitation temperature introduces a factor of ~2 uncertainty on our estimates of the masses, momenta, and momentum fluxes.

We calculated the value of $\int_{V_1}^{V_2} \int_{\rm A} T_{\rm A}^*(v)\ {\rm d}v\ {\rm d}A$ directly from our data by integrating the intensity of the $^{12}$CO(2–1) emission, both spatially over the outflow extent, and kinematically over the main LSR velocity range $[V_1; V_2]$ of each outflow. The outflow extents and main LSR velocity ranges adopted are given in Table 2.

The minimum mass of gas associated with each outflow is given in the fifth column (first value) of Table 4. The minimum total mass of gas entrained by the network of eleven outflows in NGC 2264-C is estimated to be 0.3 ± 0.15 $M_\odot$.

In order to estimate the *maximum* mass of gas entrained by the eleven outflows observed, two calculations were made.

First, for each outflow lobe, we assumed that all of the blue-shifted or red-shifted emission such as $T_{\rm outflow} > T_{\rm ref} + 3\sigma_{\rm spec}$ was due to the corresponding outflow (see Fig. 6). This hypothesis may overestimate outflow masses by including low-velocity motions due to local turbulent broadening of the ambient cloud emission. The corresponding values therefore provide upper limits to the masses of outflow-entrained gas. We also recall that, at low velocities, the $^{12}$CO(2–1) emission is no longer optically thin (see Fig. 5). Therefore, we used the values of optical depth derived previously to correct for optical depth effects on our mass estimates. The additional outflow emission at low velocities (see Col. 3 of the online Table 3 for numerical values) can be expressed as:

$$M_{\rm add} = 1.6 \times 10^{-6} \times \int_{V_2}^{V_3} \int_A \frac{\tau_v}{1 - {\rm e}^{-\tau_v}} [T_{\rm A}^*(v)|_{\rm flow} - T_{\rm A}^*(v)|_{\rm ref}] {\rm d}v\, {\rm d}A\ (M_\odot), \quad (4)$$

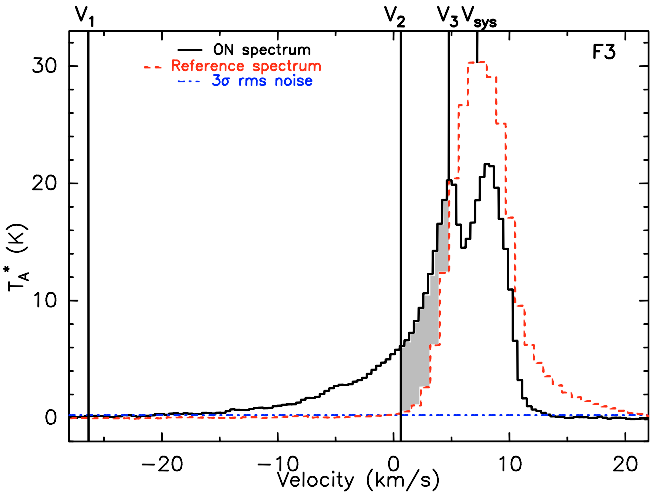


**Fig. 6.** Illustration of the velocity ranges used for the calculation of minimum and maximum masses of the outflows. The dashed spectrum shows the $^{12}$CO(2–1) reference spectrum from the ambient cloud. The solid spectrum corresponds to the candidate outflow F3. Vertical solid lines show the velocity ranges used in the computation of the outflow masses. $[V_1; V_2]$ represents the interval used for the calculation of the minimum outflow mass (see Sect. 4.1.2 for details). $[V_2; V_3]$ is the additional velocity interval used to compute $M_{\rm add}$ by integrating the excess $^{12}$CO(2–1) emission (area highlighted in grey in this case).

where $|V_2|$ is the velocity at which $T_{\rm A}^*(v)|_{\rm ref} < 3\sigma_{\rm ref}$ and $|V_3|$ the velocity at which $T_{\rm A}^*(v)|_{\rm flow} = T_{\rm A}^*(v)|_{\rm ref} - 3\sigma_{\rm spec}$ (if $T_{\rm A}^*(V_{\rm sys})|_{\rm flow} > T_{\rm A}^*(V_{\rm sys})|_{\rm ref}$ then $|V_3| = V_{\rm sys}$).

As a second step, we further took into account the material entrained by outflows down to velocities comparable to the systemic velocity of the surrounding medium. We first extracted a characteristic mean spectrum per outflow, and fitted a power law to this mean spectrum, $T_{\rm outflow} = \beta \times (v - V_{\rm sys})^\alpha$, in the velocity range $V_1 < v < V_3$. We then extrapolated the fitted profile for velocities $V_3 < v < V_{\rm sys}$, in order to estimate the amount of mass entrained at very low velocities and which remains hidden in the main body of the $^{12}$CO(2–1) line:

$$M_{\rm low} = 1.6 \times 10^{-6} \times \int_{V_3}^{V_{\rm sys}} \int_A \frac{\tau_v}{1 - {\rm e}^{-\tau_v}} [\beta \times (v - V_{\rm sys})^\alpha] {\rm d}v \times A(M_\odot), \quad (5)$$

where $V_{\rm sys}$ is the systemic velocity associated with the outflow (see Col. 2 of Table 2).

The power-law indices of the fit can be found in Col. 4 of the online Table 3. The additional mass of outflow-entrained gas at velocities between $V_3$ and the systemic velocity of the cloud $V_{\rm sys}$ is given in Col. 5 of the online Table 3. We obtained satisfactory fits for all eleven outflow lobes, except outflow F4 which exhibits a detached high-velocity emission feature (see Fig. 4). The best fits lead to a fraction of invisible, low-velocity outflow-entrained mass $M_{\rm low}/M_{\rm max}$ ~ 10–45%. Since this additional mass is moving at very low velocities (1 to 3 km s$^{-1}$ away from the systemic velocity), its contribution to the outflow dynamical parameters will nevertheless be quite small (see Sect. 4.2 below).

Finally, the maximum masses of outflow-entrained gas $M_{\rm max}$ were computed by adding the masses $M_{\rm add} + M_{\rm low}$ calculated in the velocity interval $[V_2; V_{\rm sys}]$ to the minimum masses $M_{\rm min}$ derived earlier. These maximum masses are reported in Col. 5 of Table 4 (second value). We stress that these masses represent the

**Table 3.** Estimates of the masses of outflow-entrained material at low velocities.

| OUTFLOW LOBE | Additional velocity interval $[V_2; V_3]$ (km s$^{-1}$) (1) | Additional mass $M_{\rm add}$ in $[V_2; V_3]$ ($10^{-2}$ $M_\odot$) (2) | Index of power-law fit, $\alpha$ (3) | Additional mass $M_{\rm low}$ in $[V_3; V_{\rm sys}]$ ($10^{-2}$ $M_\odot$) (4) |
|---|---|---|---|---|
| F1 (Red) | [13; 10] | 7 ± 2 | −2.7 ± 0.6 | 25 |
| F2 (Blue) | [1.1; 4.3] | 1.9 ± 0.5 | −2.5 ± 0.3 | 32 |
| F3 (Blue) | [1.4; 4.9] | 6 ± 3 | −2.3 ± 0.3 | 24 |
| F4 (Red) | [13; 10.2] | 2.3 ± 1.5 | – | – |
| F5 (Blue) | [0.3; 5] | 6 ± 2.8 | −3.1 ± 0.9 | 31 |
| F6 (Red) | [13.1; 9.9] | 5.7 ± 3.1 | −3.7 ± 0.8 | 26 |
| F7 (Red) | [14.7; 10] | 15 ± 7 | −2.8 ± 0.7 | 90 |
| F8 (Blue) | [1.7; 4.4] | 0.37 ± 0.15 | −2.4 ± 0.4 | 7 |
| F9 (Red) | [13.7; 9.6] | 1.2 ± 0.7 | −2.4 ± 0.5 | 6 |
| F10 (Red) | [13.7; 9.7] | 1 ± 0.55 | −2.5 ± 0.3 | 7 |
| F11 (Red) | [15.2; 9.5] | 30 ± 18 | −2.0 ± 0.9 | 52 |

(1) Velocity range $[V_2; V_3]$ in which $T_{\rm A}^*(v)|_{\rm ref} > 3\sigma_{\rm ref}$ and $T_{\rm A}^*(v)|_{\rm outflow} > T_{\rm A}^*(v)|_{\rm ref} - 3\sigma_{\rm ref}$.
(2) Mass obtained by integration of $[T_{\rm A}^*(v)|_{\rm outflow} - T_{\rm A}^*(v)|_{\rm ref}]$ over $[V_2; V_3]$.
(3) Power-law index of the best fit on line wings observed in $[V_1; V_3]$.
(4) Estimate of the mass which remains hidden in the main body of the line $[V_3; V_{\rm sys}]$.

**Table 4.** Derived parameters of the eleven $^{12}$CO(2–1) outflows mapped in NGC 2264-C.

| OUTFLOW LOBE | Characteristic velocity $V_{\rm char}^{\rm obs}$ (km s$^{-1}$) (1) | Length $i = 90° - i = 57.3°$ (pc) (2) | Dynamical time $i = 90° - i = 57.3°$ ($10^3$ yr) (3) | Mass ($10^{-2}$ $M_\odot$) (4) | Momentum ($M_\odot$ km s$^{-1}$) (5) | Momentum flux ($10^{-5}$ $M_\odot$ km s$^{-1}$ yr$^{-1}$) (6) |
|---|---|---|---|---|---|---|
| F1 (Red) | +9.5 | 0.49–0.58 | 24.5–15.9 | 3.7–35.7 | 0.58–1.23 | 2.4–10.2 |
| F2 (Blue) | −13 | 0.71–0.84 | 20.0–13.0 | 2.9–36.8 | 0.37–0.97 | 1.8–6.8 |
| F3 (Blue) | −11.5 | 0.27–0.32 | 7.7–4.9 | 4.2–34.2 | 0.49–1.07 | 6.3–28.3 |
| F4 (Red) | +7.6 | 0.2–0.24 | 12.8–8.2 | 0.8–3.1 | 0.06–0.14 | 0.5–3.2 |
| F5 (Blue) | −12 | 0.18–0.21 | 9.1–5.8 | 0.9–37.9 | 0.12–0.74 | 1.3–11.5 |
| F6 (Red) | +6.6 | 0.2–0.24 | 9.3–5.9 | 1.6–33.3 | 0.1–0.71 | 1.1–10.5 |
| F7 (Red) | +10.3 | 0.28–0.33 | 10.6–6.8 | 6.0–111 | 0.62–2.56 | 5.8–35.3 |
| F8 (Blue) | +10.9 | 0.14–0.16 | 4.6–2.9 | 0.5–7.8 | 0.05–0.16 | 1.2–4.4 |
| F9 (Red) | +11 | 0.2–0.24 | 8.8–5.6 | 0.6–6.8 | 0.06–0.18 | 0.7–3.4 |
| F10 (Red) | +11 | 0.18–0.21 | 7.9–5.0 | 0.5–7.4 | 0.05–0.18 | 0.7–3.4 |
| F11 (Red) | +10.8 | 0.35–0.41 | 13.5–8.64 | 11.2–93.2 | 1.21–3.12 | 8.9–55.3 |
| L1551 (7) | – | 0.65–0.77 | 48–31 | 530–670 | 18–23 | 47–136 |
| L1157 (i ~ 81°) (7) | – | 0.4 | 2.5 | 62 | 31 | 1100 |

(1) Observed characteristic offset velocity of the outflow lobe (see details in Sect. 4.2), computed over the $[V_1; V_{\rm sys}]$ velocity range.
(2) Length of each outflow lobe.
(3) Dynamical timescale of each outflow.
(4) Minimum and maximum masses of outflow-entrained gas, computed as explained in Sect. 4.1.
(5) Minimum and maximum momenta, computed as explained in Sect. 4.2.
(6) Range of momentum flux derived for each outflow (see Sect. 4.2).
(7) The last two rows give, for the sake of comparison, the values computed for the two bipolar outflows L1551 and L1157, used by Nakamura & Li (2007).

maximum possible values of the outflow masses, as the hypothesis made in their derivation led us to include all of the $^{12}$CO emission potentially due to outflows. The overall uncertainty on each of the outflow mass components ($M_{\rm min}$, $M_{\rm add}$, $M_{\rm low}$) is about a factor of two.

### 4.2. Outflow dynamical parameters

Using the mass estimates given in Col. 5 of Table 4, we first computed the momentum associated with each outflow:

$$P_{\rm flow} = M_{\rm flow} \times V_{\rm char} \quad (6)$$

where $V_{\rm char}$ is the characteristic velocity of the outflow lobe, computed as the intensity-weighted mean absolute velocity of the outflow over the relevant velocity range:

$$V_{\rm char} = \frac{V_{\rm char}^{\rm obs}}{\cos(i)} = \frac{1}{N_{\rm pix} \times \cos(i)} \sum_{\rm pixels} \frac{\sum\limits_{\Delta v} T_{\rm A}^\star(v)|v - V_{\rm sys}|}{\sum\limits_{\Delta v} T_{\rm A}^\star(v)}.$$

The inclination angle $i$ between the flow axis and the line of sight (l.o.s.) has to be taken into account when computing the true characteristic velocity $V_{\rm char}$, since it is related to the observed characteristic velocity (projected on the l.o.s.) $V_{\rm char}^{\rm obs}$ (see Col. 2. of Table 4), by $V_{\rm char} = V_{\rm char}^{\rm obs}/\cos(i)$.

We derived the outflow momentum in each of the three velocity regimes $[V_1; V_2]$, $[V_2; V_3]$, $[V_3 ; V_{\rm sys}]$ considered for the calculations of the outflow-entrained mass (cf. Sect. 4.1.2 and

**Table 5.** Global properties of the population of eleven $^{12}$CO(2–1) outflows observed in NGC 2264-C.

| $M_{\rm tot}$ ($10^{-2}\ M_\odot$) (1) | $P_{\rm tot}$ ($M_\odot$ km s$^{-1}$) (2) | $F_{\rm tot}$ ($10^{-5}\ M_\odot$ km s$^{-1}$ yr$^{-1}$) (3) | $E_{\rm tot}$ ($10^{44}$ erg) (4) | $L_{\rm tot}$ ($L_\odot$) (5) |
|---|---|---|---|---|
| 3 – 189 | 3.8–11 | 30–170 | 3.4–10 | 0.2–1.2 |

(1) Minimum and maximum total mass of outflow-entrained gas, computed from the individual outflow masses given in Table 4.
(2) Minimum and maximum total outflow momentum, computed from the individual outflow momenta given in Table 4 ($P_{\rm tot} = \sum_{\rm flows} P_{\rm flow}$).
(3) Minimum and maximum total outflow momentum flux ($F_{\rm tot} = \sum_{\rm flows} F_{\rm flow}$).
(4) Minimum and maximum total kinetic energy of the outflows.
(5) Minimum and maximum total mechanical luminosity of the outflow population.

Fig. 6). The total outflow momentum was calculated as the sum of the three momenta estimated in the three velocity regimes.

The outflow momentum flux was obtained by dividing the momentum by the estimated dynamical timescale $t_{\rm dyn}$ of the outflow:

$$F_{\rm flow} = P_{\rm flow}/t_{\rm dyn}. \quad (7)$$

The dynamical timescale, $t_{\rm dyn} = l_{\rm flow}/V_{\rm max}$, also depends on the inclination angle $i$. Indeed, $i$ affects both the estimate of the outflow length ($l_{\rm flow} = l/\sin(i)$ where $l$ is the observed projected length on the sky), and the velocity estimates since the highest intrinsic flow velocity is $V_{\rm max} = V_{\rm max}^{\rm obs}/\cos(i)$, where $V_{\rm max}^{\rm obs}$ is the highest observed velocity (corresponding to $V_1$ in Sect. 3.1). This results in an inclination correction factor $\frac{\cos(i)}{\sin(i)}$ for the dynamical timescale. Given the inclination correction on the momentum, the global inclination correction factor for the momentum flux is thus $f(i) = \frac{\sin(i)}{\cos^2(i)}$ (cf. Bontemps et al. 1996).

The results of these calculations are given in Table 4. The length of each outflow is reported in Col. 3, where the first quoted value is the observed projected length of the outflow and the second value is corrected for the mean inclination angle $i = 57.3°$. Column 4 gives the dynamical timescale of each outflow. The lower value is the apparent dynamical timescale (with no correction for inclination), while the upper value is corrected for the mean inclination angle $i = 57.3°$. The outflow momentum and momentum flux values are given in Cols. 6 and 7. The minimum quoted values were derived using the minimum mass estimates and ignoring inclination effects, i.e. assuming that the outflows had their axes along the l.o.s. The maximum values were derived using the maximum mass estimates and assuming a mean inclination angle $i \sim 57.3°$ to account for inclination effects (leading to a mean correction factor $\langle f(i)\rangle = 2.9$ for the momentum flux – cf. Bontemps et al. 1996).

We stress that the amount of outflow mass hidden at low velocities in the main body of the $^{12}$CO(2–1) line, $M_{\rm low}$, contributes only ∼1% to 5% of the maximum momentum flux computed here, due to the low velocity of this material. Therefore, thanks to the procedure adopted here to take into account the different velocity regimes of the outflows, the relatively large uncertainty in the outflow-entrained mass at low velocities results only in a small uncertainty factor for the momentum flux.

The main source of uncertainty in our momentum and momentum flux estimates comes from the hypothesis made on the inclination angle with respect to the l.o.s. . We considered that our sample of eleven outflow lobes was large enough to justify a statistical treatment and applied a mean inclination angle of $i \sim 57.3°$ assuming random outflow orientations. We estimate that this hypothesis on the inclination angle leads to a factor of ∼2 uncertainty on the individual momentum and momentum flux values. Altogether the global uncertainty on the derived momentum fluxes is roughly a factor of ∼8, which is consistent with the results of Cabrit & Bertout (1990) based on an analysis of synthetic outflow data.

Table 5 gives the total dynamical parameters of the entire population of outflows observed in NGC 2264-C obtained by summing the values computed for the eleven outflow lobes (from Table 4). The total kinetic energy contained in the eleven outflows was estimated from the total momentum as follows: $E_{\rm tot} = \sum_{\rm flows} 1/2 \times P_{\rm flow} \times V_{\rm char} \sim 3.4 \times 10^{44} - 1 \times 10^{45}$ ergs. We also estimated the rate of kinetic energy deposited by the outflows in the surrounding medium as: $L_{\rm tot} = 1/2 \times F_{\rm tot} \times V_{\rm esc}$, where $V_{\rm esc}$ is the escape velocity of the cloud $V_{\rm esc} = \sqrt{2GM_{\rm cloud}/R_{\rm cloud}} \sim 5$ km s$^{-1}$ (Stojimirović et al. 2006). In this way, we found a total mechanical luminosity $L_{\rm tot} \sim 0.21$–$1.2\ L_\odot$.

The range of values we derive for the total mass of outflow-entrained gas is in agreement with the mass values found by Margulis et al. (1988) for the whole NGC 2264-C region. The range of values we find for the overall momentum and mechanical luminosity are in agreement only with the lower values of Margulis et al. (1988). This difference is mainly due to their method, which used the maximum projected flow velocity to compute upper limits to the momentum and mechanical luminosity. Furthermore, Margulis et al. (1988) did not resolve the network of outflows in NGC 2264-C and thus used a single characteristic velocity for the eleven outflows, while our study reveals large velocity variations from outflow to outflow.

## 5. Discussion

### 5.1. Identification of driving sources

The lobes named F1 and F2 in Fig. 2 are the most elongated and best collimated outflow lobes identified in our study. F1 extends over 130″ and F2 extends over 180″, corresponding to physical lengths of 0.49 pc and 0.71 pc, respectively, assuming the outflows are perpendicular to the line of sight ($i = 90°$). The similar morphologies and relative positions of the two lobes in the map of Fig. 2 strongly suggest that F1 and F2 are physically associated and correspond to the two lobes of a single bipolar outflow. Based on Figs. 2 and 7, the best candidate driving sources for this bipolar flow are C-MM3 and C-MM13.

To determine which source is driving the (F1, F2) bipolar outflow, we constructed several position-velocity (PV) diagrams along the axis of the flow, assuming various barycenters and orientations for the outflow. Figure 8 shows the best (most symmetric) position-velocity diagram we found. This PV diagram was constructed along an outflow axis passing through C-MM13 and defined by a position angle of 12° (east of north) on the plane of

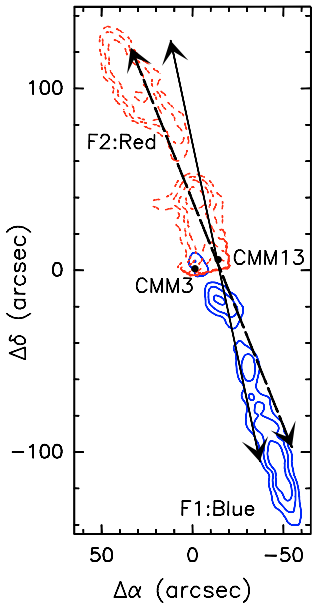


**Fig. 7.** Blow up of the $^{12}$CO(2–1) map of Fig. 2 toward the (F1, F2) bipolar outflow in the central part of the NGC 2264-C protocluster. The full contours show the integrated intensity in the blue-shifted part of CO(2–1) line (from 1 to −27 km s$^{-1}$). Contours range from 5 to 98 K km s$^{-1}$. The dashed contours are levels of CO(2–1) integrated intensity in the red-shifted part of the line (from 13 to 28.5 km s$^{-1}$), and contours range from 5 to 110 K km s$^{-1}$. Markers refer to the positions of millimeter continuum peaks C-MM3 and C-MM13. The solid line arrow marks the direction of the bipolar outflow made up by F1 and F2, at a position angle of 12° (east of north). The dashed line arrow marks the direction of the (F1, F2) bipolar outflow, at a position angle of 22°. This corresponds to the range of outflow axes for which the most symmetric PV diagrams are obtained (see Fig. 8).

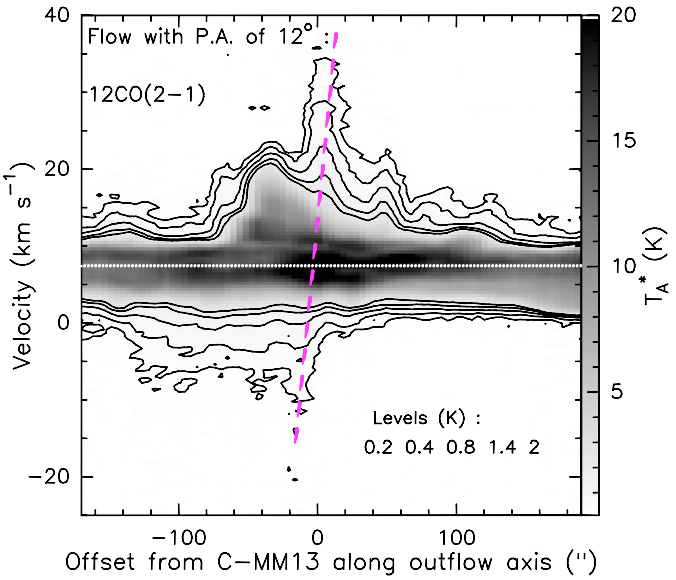


**Fig. 8.** Position-velocity diagram of the (F1, F2) bipolar flow, constructed along an axis passing through C-MM13 (offset 0″) and defined by a position angle of 12° in the plane of the sky, and oriented from south to north (see Fig. 7). The dotted horizontal line represents the value of the systemic velocity observed at the center of the protocluster. The dashed line in red represents the best symmetry axis for the highest velocity emission. Note that most of the red-shifted velocity occurring at negative offsets (i.e. southern) is due to outflow F11 and is unrelated to (F1, F2). If we ignore this F11 emission feature, the red-shifted and blue-shifted high-velocity components seen in the diagram exhibit a symmetric pattern with respect to offset 0″ (intersection of the dotted and dashed lines), which corresponds to the position of the protostellar core C-MM13.

the sky. Note that the PV diagrams constructed for position angles between 12° and 22° are nearly indistinguishable. Figure 7 indicates the range of possible outflow axes based on our PV-diagram study. It is clear from Fig. 8 that the highest-velocity emission (±20 km s$^{-1}$ with respect to the systemic velocity) is detected in the immediate vicinity of the protostellar core C-MM13, and that this high-velocity emission presents a very high level of symmetry about C-MM13. On this basis, we conclude that C-MM13 is the most likely driving source of the bipolar outflow made up by lobes F1 and F2.

One possible explanation for the slight misalignment between the outflow features located close to C-MM13 and their more distant counterparts (see Fig. 7) is that the protostellar jet driving the (F1, F2) outflow precesses with time (Gueth et al. 1998). High-velocity features located farther away from the driving source, which presumably correspond to older ejection events, would then indicate a different outflow direction than that indicated by the high-velocity features located closer to C-MM13.

Based on spatial coincidence and absence of confusion (see Fig. 2), we also believe that the blue-shifted lobe F3 is driven by the millimeter source C-MM2 and that the red-shifted lobe F4 is related to C-MM1. The seven other lobes are either too poorly collimated (e.g. red-shifted lobe F11), too far away from the protostellar clump (e.g. red-shifted lobe F6), or too blended with other lobes to be directly associated with any particular Class 0-like object.

The outflow lobe F4 exhibits a compact (~0.03 pc) $^{12}$CO emission peak at $v_{\rm LSR}$ ~ +18 km s$^{-1}$, corresponding to a projected velocity offset ~+11 km s$^{-1}$ from the systemic velocity (see Fig. 4). No emission is seen at $v_{\rm LSR}$ = +18 km s$^{-1}$ in our $^{13}$CO data, ruling out a background cloud origin for the $^{12}$CO peak. Such a discrete $^{12}$CO emission feature, well defined in both space and velocity, is reminiscent of the high-velocity molecular "bullets" observed toward some young outflows driven by Class 0 objects such as the L1448-C bipolar flow (Bachiller et al. 1990).

We also stress that there is evidence for at least two well-collimated outflows in NGC 2264-C: the first one is the (F1, F2) pair which is very likely driven by CMM-13, while the second one is the outflow lobe F10 which is also well collimated but of unidentified origin. Given that the best collimated CO outflows are generally detected toward the youngest protostellar objects (André et al. 1990; Bachiller 1996), these highly-collimated outflows further testify to the presence of extremely young (Class 0) protostellar objects in the NGC 2264-C protocluster.

### 5.2. Properties of the driving sources and comparison with well-studied outflows

We now discuss the properties of the three protostellar driving sources identified in the previous section : C-MM1, C-MM2, and C-MM13.

#### 5.2.1. Source properties

We used *Spitzer*/MIPS data at 70 $\mu$m, APEX/P-ArTéMiS data at 450 $\mu$m (see Fig. 1b), and IRAM 30m MAMBO data at 1.2 mm (Peretto et al. 2006) to estimate the bolometric

**Table 6.** Properties of the sources : C-MM1, C-MM2, C-MM13, and C-MM3.

| Core | Outflow lobe | $M_{\rm env}$ ($M_\odot$) | $L_{\rm bol}$ ($L_\odot$) | $F_{\rm flow}$ ($10^{-5}$ $M_\odot$ km s$^{-1}$ yr$^{-1}$) |
|---|---|---|---|---|
| C-MM1 | F4 | $6.2\,^{+6.2}_{-3.1}$ | $7 \pm 3$ | 0.5–3.2 |
| C-MM2 | F3 | $5.5\,^{+5.5}_{-2.7}$ | $11 \pm 3$ | 6.3–28.3 |
| C-MM13 | (F1, F2) | $7.6\,^{+7.6}_{-3.8}$ | $8.6 \pm 5$ | 4.2–16.6 |
| C-MM3 | – | $15.2\,^{+15.2}_{-7.6}$ | $50 \pm 10$ | – |

luminosities ($L_{\rm bol}$) of C-MM1, C-MM2 and C-MM13. We could directly measure 70 $\mu$m and 450 $\mu$m flux densities for the relatively isolated sources C-MM1 and C-MM2 and we then estimated their bolometric luminosities using the online tool devised by Robitaille et al. (2007) to fit the spectral energy distributions of young stellar objects (YSOs). Unfortunately, due to the presence of the bright young star IRS1 (see Fig. 1) in the field, it was impossible to derive a flux from the *Spitzer*/MIPS data for C-MM13. We could nevertheless obtain a MIPS 70 $\mu$m flux density and a bolometric luminosity for the neighboring source C-MM3 (∼13.5″ away from C-MM13). We then derived a luminosity estimate for C-MM13 assuming that the bolometric luminosity ratio $L_{\rm bol}^{\rm C-MM13}/L_{\rm bol}^{\rm C-MM3}$ was equal to the 450 $\mu$m flux density ratio $F_{450\,\mu m}^{\rm C-MM13}/F_{450\,\mu m}^{\rm C-MM3}$. We stress that the bolometric luminosity derived in this way for C-MM13 is more uncertain than the $L_{\rm bol}$ estimates obtained for C-MM1 and C-MM2.

Our bolometric luminosity estimates for the three identified driving sources are listed in Table 6. We also give the envelope masses ($M_{\rm env}$) of these protostellar objects as measured by Peretto et al. (2007) with the IRAM Plateau de Bure interferometer on ∼3000 AU scales.

The protostellar sources C-MM1, C-MM2, C-MM3 and C-MM13 were then placed in an $M_{\rm env}$–$L_{\rm bol}$ diagram (see Fig. 9) similar to the ones presented by André et al. (2000, 2008). Model evolutionary tracks are shown, computed by assuming each protostar forms from a bounded condensation of finite initial mass $M_{\rm env}(0)$ and has $L_{\rm bol} = GM_\star(t)\dot{M}_{\rm acc}(t)/R_\star(t) + L_\star(t)$, where $R_\star$ is the protostellar radius and $L_\star$ the interior stellar luminosity (Stahler 1988; Hosowaka & Omukai 2008). The mass accretion rate and the envelope mass were assumed to be related by $\dot{M}_{\rm acc}(t) = \epsilon M_{\rm env}(t)/\tau$, where $\epsilon = 50\%$ is the typical star formation efficiency for individual cores (Matzner & McKee 2000), and $\tau = 10^5$ yr is the characteristic timescale of protostellar evolution, leading to $\dot{M}_{\rm acc}(t)$ and $M_{\rm env}(t)$ functions declining exponentially with time (see Bontemps et al. 1996). The positions of C-MM1, C-MM2, C-MM3 and C-MM13 in this diagram demonstrate that they are bona fide Class 0 objects. Moreover, comparison with the model evolutionary tracks suggests that these objects will form stars with main-sequence masses $M_\star^{\rm final} \sim$ 2–8 $M_\odot$.

### 5.2.2. Comparison with other outflows from the literature

Here, we compare the properties of the three outflows (F1, F2), F3, and F4 with those of several protostellar outflows from the literature.

Bontemps et al. (1996) carried out a study of outflow energetics for a sample of 45 low-luminosity YSOs including both Class I and Class 0 objects. They found that outflows from younger sources were more powerful. The outflow momentum flux values we find here, namely a few $10^{-5}$ $M_\odot$ km s$^{-1}$ yr$^{-1}$, are very similar to the momentum fluxes of the Class 0

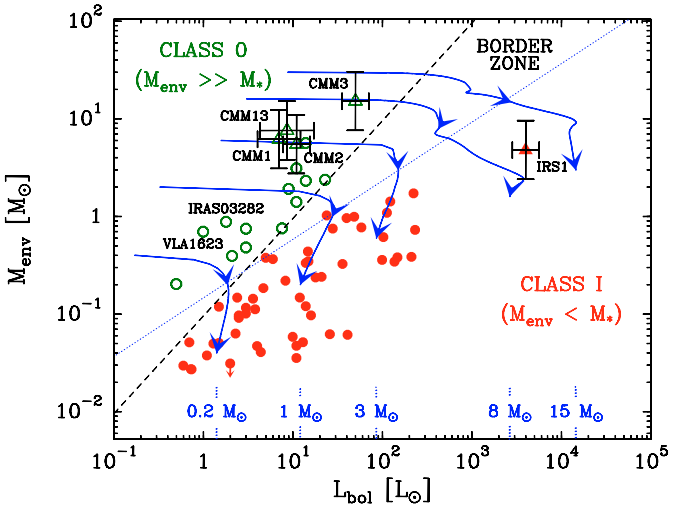


**Fig. 9.** Envelope mass versus bolometric luminosity diagram comparing the locations of the protostellar sources of NGC 2264-C (open triangles with error bars) with the positions of low-mass Class I (filled circles) and Class 0 objects (open circles) (from André et al. 2000). Model evolutionary tracks, computed for various final stellar masses $M_\star^{\rm final}$, are shown. The dashed and dotted lines are two $M_{\rm env} - L_{\rm bol}$ relations marking the conceptual border zone between the Class 0 ($M_{\rm env} > M_\star/\epsilon$) and the Class I ($M_{\rm env} < M_\star/\epsilon$) stages, where $\epsilon \approx 50\%$ is the local star formation efficiency (see André et al. 2008, for details).

outflows in the Bontemps et al. sample (see Fig. 10). The left panel of Fig. 10 plots outflow momentum flux versus driving source luminosity, while the right panel shows $F_{\rm flow}c/L$ versus $M_{\rm env}/L_{\rm bol}^{0.6}$ (see Bontemps et al. 1996, for details). Figure 10 shows that C-MM1, C-MM2, and C-MM13 drive outflows which are typical of low- to intermediate-mass Class 0 objects and closely follow the trend established by Bontemps et al. (1996).

We can also compare the properties of the outflows mapped in NGC 2264-C with the two molecular outflows used as references by Nakamura & Li (2007) to estimate the typical outflow momentum to be injected in their numerical simulations.

The first one is the well-documented outflow driven by the border-line Class I/Class 0 object L1551 IRS 5. Stojimirović et al. (2006) showed that the L1551 IRS 5 bipolar outflow extends over 1.3 pc and drives a total momentum of ∼17.8–23 $M_\odot$ km s$^{-1}$. The dynamical parameters of the L1551 outflow, as re-estimated by us from the results of Stojimirović et al. (2006) for consistency with the present study, are reported in Table 4 (see also Fig. 10). We note that the momentum flux injected by the L1551 outflow in the surrounding medium is of the same order as the momentum flux of the strongest outflow observed in the NGC 2264-C protocluster (F11).

The second reference outflow used by Nakamura & Li (2007) is the one driven by the low-luminosity Class 0 protostar L1157-MM (e.g. Umemoto et al. 1992; Bachiller et al. 2001). The dynamical parameters of the L1157 outflow are also reported in Table 4 and used in Fig. 10. It can be seen in Fig. 10 that the L1157 outflow is characterized by a very high momentum flux. None of the outflows mapped in the NGC 2264-C protocluster drives that much momentum flux in the surrounding medium, and even the combined effects of the eleven outflows in NGC 2264-C inject at most $F_{\rm tot} \sim 1.7 \times 10^{-3}$ $M_\odot$ km s$^{-1}$ yr$^{-1}$ (see Table 5), i.e. one tenth of what is found for the L1157 outflow alone. Therefore, we conclude that L1157-MM represents an extreme case of a Class 0 outflow.

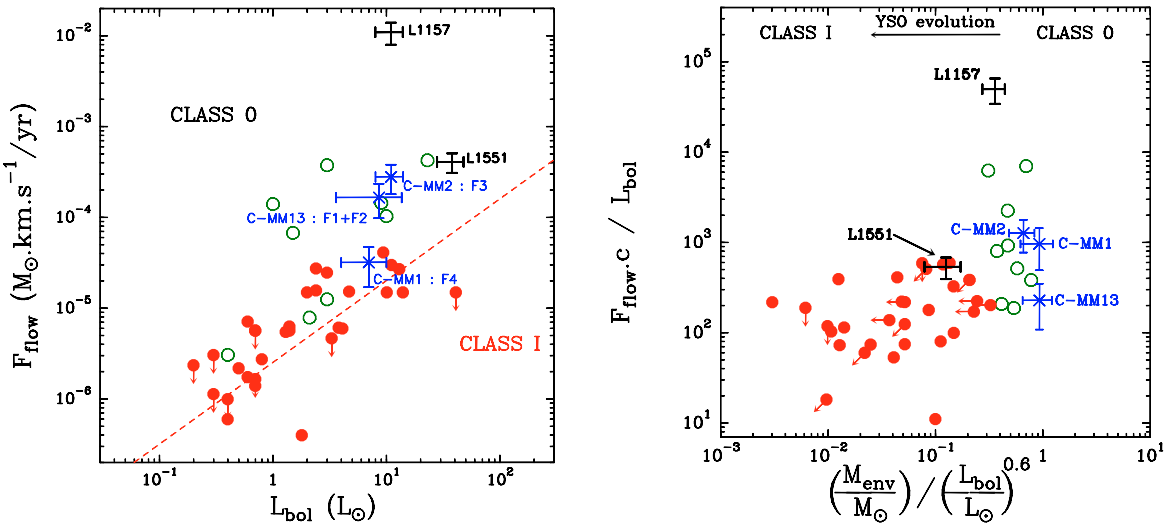


**Fig. 10.** CO momentum flux $F_{\rm flow}$ versus bolometric luminosity (*left*), and $F_{\rm flow}c/L$ versus $M_{\rm env}/L_{\rm bol}^{0.6}$ (*right*). The three candidate Class 0 objects identified as the driving sources of the outflows (F1, F2), F3 and F4 in NGC 2264-C are shown as blue stars. For comparison, the Class 0 and Class I objects studied by Bontemps et al. (1996) are shown as open and filled circles, respectively. The driving sources of the two molecular outflows taken as references by Nakamura & Li (2007) are shown by black error bars.

We also note that the total momentum flux derived here (Table 5) for the network of eleven outflows in NGC 2264-C is similar to the total outflow momentum flux found by Knee & Sandell (2000) in the NGC 1333 protocluster.

### 5.3. Outflows as a source of turbulence and support

#### 5.3.1. Observed turbulence vs outflow contribution

We now discuss whether or not the eleven outflows mapped in NGC 2264-C are likely to contribute a significant fraction of the turbulence observed in the protocluster.

From our $^{13}$CO mapping, we determined a one-dimensional velocity dispersion $\sigma_v \sim 1.7$ km s$^{-1}$, measured on the mean $^{13}$CO(2–1) spectrum over the NGC 2264-C clump (radius $R \sim 0.7$ pc). If we place NGC 2264-C in the linewidth-size diagram representing Larson's first scaling law (Larson 1981), we find that NGC 2264-C exhibits a velocity dispersion about twice as large as what is expected from the classical linewidth-size relationship observed in giant molecular clouds (GMCs) (Solomon et al. 1987). This suggests that NGC 2264-C is more turbulent than the CO clouds considered by Solomon et al. (1987). However, Heyer et al. (2008) recently re-examined Solomon's results with new $^{13}$CO data and found the relationship $\sigma_v = \sqrt{\pi G\Sigma/5} \times R^{1/2}$, which shows that the normalization of Larson's first scaling law depends on the mean surface density $\Sigma$ of the clouds. From the 1.2 mm dust continuum observations of Peretto et al. (2006) we estimate a mean surface density of ~3000 $M_\odot$ pc$^{-2}$ for the NGC 2264-C cluster-forming clump, which is much higher than the mean surface density ~170 $M_\odot$ pc$^{-2}$ of the CO clouds following the classical linewidth-size relation. The location of NGC 2264-C in the $\sigma_v/R^{0.5} = f(\Sigma)$ diagram of Heyer et al. (2008) is nevertheless similar to that of the densest clouds discussed by these authors. We also note that both the $N_2H^+$ (Peretto et al. 2006) and $^{13}$CO (this work) linewidths of NGC 2264-C are consistent with the $\log(\Delta v) = 0.23 + 0.21 \times \log(R)$ correlation found by Caselli & Myers (1995) for massive cloud cores in Orion. Therefore, although NGC 2264-C exhibits broader linewidths than those expected from Larson's classical linewidth-size relation, it exhibits the same level of turbulence as that generally found in massive clouds and cores.

Next, we can estimate the rate of turbulent energy dissipation in the NGC 2264-C clump using Eq. (7) of Mac Low (1999). From the 1.2 mm dust continuum map obtained by Peretto et al. (2006), a total gas mass of 2300 $M_\odot$ can be derived within a radius of 0.7 pc. Using the velocity dispersion derived from our $^{13}$CO observations, we find:

$$L_{\rm turb} \sim \frac{1/2 \times M\sigma_v^2}{R/\sigma_v} \sim 1.2\ L_\odot. \quad (8)$$

For comparison, the total mechanical power due to the eleven outflows in NGC 2264-C is $L_{\rm tot} = 0.7 \pm 0.5\ L_\odot$ (see Sect. 4.2). We conclude that the network of protostellar outflows observed in NGC 2264-C can contribute a very significant, if not dominant, fraction of the turbulence observed in the protocluster.

#### 5.3.2. Gravitational collapse vs. outflow support

In order to determine whether the force exerted by the outflows on NGC 2264-C can slow down or even stop the global collapse of the protocluster, we first estimate the force needed to keep the whole protocluster in hydrostatic equilibrium.

The pressure gradient needed to balance the gravitational acceleration $a_{\rm grav}(r) = GM(r)/r^2$ at radius $r$ and keep a spherical clump with a mass distribution $M(r)$ in hydrostatic equilibrium is:

$$\frac{{\rm d}P_{\rm grav}}{{\rm d}r} = -G\frac{\rho(r).M(r)}{r^2}\cdot \quad (9)$$

Assuming a density distribution of the form $\rho(r) = \frac{\sigma^2}{2\pi G r^2}$, this corresponds to a supporting pressure $P_{\rm grav}(R) = G{\times}M(R)^2/8\pi R^4$ for the spherical shell of radius $R$ enclosing a mass $M(R) = 2\sigma^2 R/{\rm G}$.

Therefore, the total force needed to balance gravity at radius $R$ in the NGC 2264-C protocluster is:

$$F_{\rm grav}(R) = P_{\rm grav}(R) \times 4\pi R^2 = G \times M(R)^2/2R^2. \quad (10)$$

The corresponding gravitational binding energy is

$$E_{\rm grav}(R) = -G \times M(R)^2/R. \quad (11)$$

If we adopt $R_1$= 0.4 pc and $M(R_1)$ = 1600 $M_\odot$, we find: $F_{\rm grav}$ = 40×10$^{-3}$ $M_\odot$ km s$^{-1}$ yr$^{-1}$, and $a_{\rm grav}$ = 50 km s$^{-1}$ Myr$^{-1}$ ∼ 50 pc Myr$^{-2}$.

If we adopt $R_2$ = 0.7 pc and $M(R_2)$ = 2300 $M_\odot$, we find: $F_{\rm grav}$ = 23×10$^{-3}$ $M_\odot$ km s$^{-1}$ yr$^{-1}$, and $a_{\rm grav}$ = 20 km s$^{-1}$ Myr$^{-1}$ ∼ 20 pc Myr$^{-2}$.

Comparing $F_{\rm grav}$ to our upper estimate of the force exerted by outflows on the NGC 2264-C protocluster, $F_{\rm tot}$ = 1.7 × 10$^{-3}$ $M_\odot$ km s$^{-1}$ yr$^{-1}$ (see Sect. 4.2), we find that the eleven observed outflows fall short by a factor ∼25 to provide significant support against collapse in NGC 2264-C.

We also note that the turbulent acceleration (cf. Matzner 2007):

$$a_{\rm turb} = \left| \frac{\nabla(\rho\sigma_{\rm v}^2)}{\rho} \right| \sim \sigma_{\rm v}^2/R \quad (12)$$

is only $a_{\rm turb}$ ∼ 4.7 km s$^{-1}$ Myr$^{-1}$ at radius $R$ = 0.7 pc, which is ∼4–5 times lower than the gravitational acceleration derived at the same radius. Therefore, the enhanced level of turbulence observed in NGC 2264-C (cf. Sect. 5.3.1) is also insufficient to support the clump against global collapse.

From an energetic point of view, the total kinetic energy (see $E_{\rm tot}$ in Table 5) derived in Sect. 4.2 for the eleven outflows is nearly three orders of magnitude lower than the gravitational binding energy of the NGC 2264-C cluster-forming clump ($E_{\rm grav}$ ∼ 5.5 × 10$^{47}$ erg). Stojimirović et al. (2006) showed that the kinetic energy injected by the L1551-IRS5 outflow in the surrounding medium was comparable to the binding energy of the L1551 cloud itself. The kinetic energy they derived from the L1551 outflow (1.5 × 10$^{45}$ erg) is comparable to our upper estimate of the total kinetic energy of the outflow population in NGC 2264-C (see Table 5), but the L1551 cloud is much less massive (110 $M_\odot$) than NGC 2264-C for an equivalent volume (radius of 0.5 pc). Likewise, we find that the total mass of outflow-entrained material represents only 0.25% of the mass of the NGC 2264-C protocluster, whereas the IRS5 outflow represents ∼5% of the total mass of the L1551 cloud.

For comparison, the rate of gravitational energy release due to global collapse is:

$$L_{\rm grav} = -\frac{{\rm d}E_{\rm grav}}{{\rm d}t} = -\left(GM(R)^2/R^2\right)\dot{r} = |E_{\rm grav}|\,\frac{V_{\rm infall}}{R} \sim 15\,L_\odot, \quad (13)$$

in the NGC 2264-C, where we have used the large-scale infall velocity $V_{\rm infall}$ = 1.3 km s$^{-1}$ measured by Peretto et al. (2006). This is a factor of ∼15–20 greater than both the total mechanical power of the observed outflows (cf. Sect. 4.2) and the rate of turbulent energy dissipation in the clump (cf. Sect. 5.3.1).

We conclude that neither the direct force exerted by the network of observed protostellar outflows, nor the turbulence they produce, can support the cluster-forming clump against global collapse at the present time. Therefore, the additional source of support against gravity, not included in the purely hydrodynamic simulations of Peretto et al. (2007) but needed to account for the observed characteristics of NGC 2264-C (see end of Sect. 1.2), cannot find its origin in protostellar feedback. Although little is known about magnetic fields in the region, the most plausible remaining hypothesis is that the missing support is magnetic in character. In any case, gravitational contraction seems to largely dominate the physics of the NGC 2264-C clump and may even be the main source of the high level of turbulence observed in the protocluster (see also Peretto et al. 2006).

### 5.4. Caveats

We recall that there is a factor of ∼8 uncertainty on the outflow momentum flux values given in Table 4 (see Sect. 4.2). This uncertainty is mainly due to the uncertain excitation temperature of the $^{12}$CO(2–1) transition and the unknown inclination angles of the outflows. Here, we explore other effects which may have led us to underestimate the energy injected by outflows in the NGC 2264-C protocluster.

First, our $^{12}$CO(2–1) mapping survey may have missed some outflows, due to its limited sensitivity. We had a sensitivity limit of ∼0.1 K in our $^{12}$CO(2–1) observations of NGC 2264-C. For a typical outflow with a characteristic velocity of ±10 km s$^{-1}$ (with respect to the systemic velocity) and a dynamical timescale of 10$^4$ years, this corresponds to a momentum flux sensitivity of ∼0.2 × 10$^{-5}$ $M_\odot$ km s$^{-1}$ yr$^{-1}$.

A rough estimate indicates that 225 additional outflows as powerful as the (F1, F2) bipolar flow, or 4 outflows as energetic as the L1551 outflow, would be needed in order to balance gravity in NGC 2264-C (see Sect. 5.2.2). The sensitivity of our $^{12}$CO(2–1) survey is such that we could not have missed such strong outflows. Nevertheless, a large number of fainter, undetected outflows driven by low-mass objects may be present in the protocluster.

According to Peretto et al. (2007), the NGC 2264-C protocluster contains seven Class 0-like objects with envelope masses ranging from 4 $M_\odot$ to 16 $M_\odot$. Based on the $M_{\rm env}$–$L_{\rm bol}$ diagram shown in Fig. 9, we estimate that these seven protostellar objects are the progenitors of stars with main-sequence masses in the range 2 $M_\odot \lesssim M_\star^{\rm final} \lesssim 8\ M_\odot$ (see Sect. 5.2.1). If the population of protostellar objects in the NGC 2264-C protocluster follows the Kroupa (2001) IMF, then we expect ∼250 protostellar objects with final stellar masses $M_\star^{\rm final}$ in the range 0.01 $M_\odot \lesssim M_\star^{\rm final} \lesssim 2\ M_\odot$. Assuming these 250 objects lie in the border zone between the conceptual Class 0 and Class I stages and have $M_{\rm env} \sim M_\star^{\rm final}$, we infer that ∼10 of them have envelope masses $M_{\rm env}$ in the range 1 $M_\odot \lesssim M_{\rm env} \lesssim 2\ M_\odot$, ∼110 of them have 0.1 $M_\odot \lesssim M_{\rm env} \lesssim 1\ M_\odot$, and ∼130 of them have 0.01 $M_\odot \lesssim M_{\rm env} \lesssim 0.1\ M_\odot$ in NGC 2264-C.

Following Bontemps et al. (1996), we adopt the following relation between outflow momentum flux and protostellar enveloppe mass: $\log(F_{\rm flow}) = -4.15 + 1.1\times \log(M_{\rm env})$. From this relation, we estimate that the ∼250 low-mass protostellar objects mentioned earlier can generate a total momentum flux of ∼3.3 × 10$^{-3}$ $M_\odot$ km s$^{-1}$ yr$^{-1}$. Therefore, even if we account for the effect of weak, undetected outflows driven by low-mass protostellar objects, the total outflow momentum flux injected in NGC 2264-C is only $F_{\rm max}$ ∼ 5 × 10$^{-3}$ $M_\odot$ km s$^{-1}$ yr$^{-1}$, which is still a factor of ∼8 lower than the force needed to support the clump against global collapse.

Second, our $^{12}$CO(2–1) map of NGC 2264-C provides only a snapshot of outflow activity in the protocluster. Given that the characteristic timescale of protostellar evolution is $\tau$ ∼ 10$^5$ years, we can estimate the total momentum $P_{\rm max}$ injected by protostellar outflows over their entire lifetime. Bontemps et al. (1996) showed that outflow momentum flux is roughly proportional to protostellar envelope mass, i.e., $F_{\rm flow}$ decreases as $M_{\rm env}$ decreases and protostars evolve from Class 0 to Class I objects. Furthermore, the linear correlation $F_{\rm flow} \propto M_{\rm env}$ is suggestive of a simple overall accretion/ejection history according to which $M_{\rm env}$, $F_{\rm flow}$, and the mass accretion rate, $\dot{M}_{\rm acc}$, all

decline exponentially with time (see Bontemps et al. 1996). We thus computed the total momentum as:

$$P_{\rm max} = \int_0^{+\infty} F_{\rm max} \times {\rm e}^{-t/\tau}\, {\rm d}t = F_{\rm max} \times \tau. \quad (14)$$

Using the value of the total momentum flux which includes the contribution from the low-mass protostellar population, we find $P_{\rm max} = 500\ M_\odot\,{\rm km\,s^{-1}}$. If we consider a total number $N_{\rm max} = 256$ of protostellar objects in NGC 2264-C (including the low-mass protostellar population) and adopt a mean stellar mass $\langle m_\star \rangle = 0.2\ M_\odot$ for the Kroupa (2001) IMF, then we find that the mean momentum per unit stellar mass is: $P_\star = P_{\rm max}/(N_{\rm max} \times \langle m_\star \rangle) \sim 10\ {\rm km\,s^{-1}}$. We conclude that, on average, the NGC 2264-C protocluster exhibits a mean outflow momentum per stellar mass which is only ~1/5 of the value Nakamura & Li (2007) used in their numerical simulations.

It should be also pointed out that the star formation rate within the NGC 2264-C clump may increase in the near future. Using a global mass inflow rate $\dot{M}_{\rm inf} \sim 3 \times 10^{-3}\ M_\odot\,{\rm yr^{-1}}$ for the collapsing clump (Peretto et al. 2006), we predict a star formation rate $SFR = \epsilon \times \dot{M}_{\rm inf} \sim 1.5 \times 10^{-3}\ M_\odot\,{\rm yr^{-1}}$, where $\epsilon = 50\%$ is the typical star formation efficiency for individual cores (Matzner & McKee 2000). Such a star formation rate would lead to a momentum injection rate of the corresponding outflows $SFR \times P_\star \sim 15 \times 10^{-3}\ M_\odot\,{\rm km\,s^{-1}\,yr^{-1}}$. This value remains lower than, but of the same order as, the force needed to support the clump against global collapse. This suggests that if NGC 2264-C undergoes a burst of star formation in the near future as a result of its global collapse, then feedback due to protostellar outflows may eventually become sufficient to slow down and halt the collapse of the clump.

## 6. Summary and conclusions

We carried out a high-resolution $^{12}$CO(2–1) survey of NGC 2264-C with the IRAM 30 m telescope in an effort to take a quantitative census of protostellar outflows in this collapsing cluster-forming clump. Additional mapping observations were also taken in $^{13}$CO(2–1) and C$^{18}$O(2–1). Our main results and conclusions can be summarized as follows:

1. We detected a network of eleven CO(2–1) outflow lobes with characteristic projected velocities between ~10 km s$^{-1}$ and ~30 km s$^{-1}$, lengths between ~0.2 pc and ~0.8 pc, momenta between ~0.1 $M_\odot$ km s$^{-1}$ and ~3 $M_\odot$ km s$^{-1}$, and momentum fluxes between $\sim 0.5 \times 10^{-5}\ M_\odot\,{\rm km\,s^{-1}\,yr^{-1}} \sim 50 \times 10^{-5}\ M_\odot\,{\rm km\,s^{-1}\,yr^{-1}}$.
2. One pair of high-velocity CO(2–1) lobes corresponds to a highly-collimated bipolar flow, whose most likely driving source is the millimeter continuum object C-MM13 located very close to the center of mass of the NGC 2264-C protocluster. Two other CO(2–1) outflow lobes appear to be driven by the millimeter continuum objects C-MM1 and C-MM2. The driving sources of the seven other outflow lobes have not been identified.
3. The three outflows with identified driving sources have properties that are typical of the flows observed toward low- to intermediate-mass Class 0 protostars. Based on their positions in the $M_{\rm env}$–$L_{\rm bol}$ evolutionary diagram for protostars, we confirm that the sources C-MM1, C-MM2, C-MM3 and CMM13 are bona-fide Class 0 objects, which will form intermediate-mass stars with $M_\star^{\rm final} \sim 2$–$8\ M_\odot$.
4. The total mechanical power associated with the network of eleven outflows, $L_{\rm tot} = 0.7 \pm 0.5\ L_\odot$, is large enough to contribute a significant, if not dominant, fraction of the turbulence observed in the NGC 2264-C cluster-forming clump.
5. However, even if we account for weak, undetected outflows driven by low-mass protostellar objects and below the sensitivity limit of our CO(2–1) survey, the total momentum flux generated by the entire outflow population in the protocluster, $F_{\rm max} \sim 5 \times 10^{-3}\ M_\odot\,{\rm km\,s^{-1}\,yr^{-1}}$, falls short by nearly an order of magnitude to provide sufficient support against global collapse of the clump at the current epoch. Therefore, the additional support against gravity missing in the hydrodynamic simulations of NGC 2264-C by Peretto et al. (2007), cannot arise from protostellar feedback, and most likely originates in magnetic fields.
6. We conclude that gravitational contraction largely dominates the physics of the NGC 2264-C clump at the present time and may even be the main source of turbulence in the protocluster. Given the early stage of evolution of the protocluster and its global collapse, it is nevertheless plausible that the star formation rate will increase in the future, up to a point where the feedback due to protostellar outflows becomes sufficient to halt the large-scale, global contraction of the protocluster.

*Acknowledgements.* We thank the referee, Rafael Bachiller, for useful comments which helped us improve the clarity of the paper. We are grateful to the ArTéMiS team whose dedication made the P-ArTéMiS mapping of NGC 2264-C (Fig. 1b) possible as part of ESO program 080.C-0722 on APEX. The work presented in this paper was stimulated by discussions held during the Star Formation Workshop organized by Hsien Shang and Nagayoshi Ohashi at ASIAA-TIARA, Taiwan, in December 2005.

## References

Adams, F. C., & Fatuzzo, M. 1996, ApJ, 464, 256
Adams, F. C., & Myers, P. C. 2001, ApJ, 553, 744
André, Ph., Martin-Pintado, J., Despois, D., & Montmerle, T. 1990, A&A, 236, 180
André, Ph., Ward-Thompson, D., & Barsony, M. 2000, in Protostars and Planets IV, ed. V. Mannings et al., 59
André, Ph., Minier, V., Gallais, P., et al. 2008, A&A, 490, 27
Arce, H. G., & Goodman, A. A. 2001, ApJ, 554, 132
Bachiller, R. 1996, in ARA&A, 34, 111
Bachiller, R., Cernicharo, J., Martin-Pintado, J., Tafalla, M., & Lazareff, B. 1990, A&A, 231, 174
Bachiller, R., Martin-Pintado, J., & Fuente, A. 1993, ApJ, 417, 45
Bachiller, R., Pérez Gutiérrez, M., Kumar, M. S. N., & Tafalla, M. 2001, A&A, 372, 899
Bally, J., Devine, D., & Reipurth, B. 1996, ApJ, 473, 49
Banerjee, R., Klessen, R., & Fendt, C. 2007, ApJ, 668, 1028
Bate, M. R., Bonnell, I. A., & Bromm, V. 2003, MNRAS, 339, 577
Bonnell, I. A., Clarke, C., Bate, M., & Pringle, J. 2001, MNRAS, 324, 573
Bontemps, S., André, Ph., Terebey, S., & Cabrit, S. 1996, A&A, 311, 858
Cabrit, S., & Bertout, C. 1990, ApJ, 348, 530
Carpenter, J. M. 2000, ApJ, 120, 139
Caselli, P., & Myers, P. C. 1995, ApJ, 446, 665
Chackerian, C., Guelachvili, G., & Tipping, R. H. 1983, JQSRT, 30, 107
Chandrasekhar, S. 1951, in Proceedings of a topical symposium, commemorating the 50th anniversary of the Yerkes Observatory and half a century of progress in astrophysics, ed. J. A. Hynek, 598
Clarke, C. J., Bonnell, I. A., & Hillenbrand, L. A., in Protostars and Planets IV, ed. V. Mannings et al., 151
Cunningham, A., Frank, A., Quillen, A., & Blackman, E. 2006, ApJ, 653, 416
Elmegreen, B. 1997, ApJ, 486, 944
Emerson, J. P., Harris, S., Jennings, R. E., et al. 1984, ApJ, 278, 49
Frerking, M. A., Langer, W. D., & Wilson, R. W. 1982, ApJ, 262, 590
Goldsmith, P. F., Snell, R. L., Hemeon-Heyer, M., & Langer, W. D. 1984, ApJ, 286, 599
Gueth, F., Guilloteau, S., & Bachiller, R. 1998, A&A, 333, 287
Hennebelle, P., & Chabrier, G. 2008, ApJ, 684, 395

Heyer, M., Krawczyk, C., Duval, J., & Jackson, J. M. 2008, ApJ, [arXiv:0809.1397]
Hillenbrand, L. A., & Carpenter, J. M. 2000, ApJ, 540, 236
Hosowaka, T., & Omukai, K. 2008, ApJ, [arXiv:0806.4122]
Johnstone, D., Wilson, C. D., Moriarty-Schieven, G., et al. 2000, ApJ, 545, 327
Knee, L. B. G., & Sandell, G. 2000, A&A, 361, 671
Kroupa, P. 1995, MNRAS, 277, 1522
Kroupa, P. 2001, MNRAS, 322, 231
Krumholz, M., & Tan, J. 2007, ApJ, 654, 304
Lada, C. J., & Lada, E. 2003, ARA&A, 41, 57
Lada, C. J., Young, E. T., & Greene, T. P. 1993, ApJ, 408, 471
Larson, R. B., MNRAS, 194, 809
Mac Low, M. -M. 1999, ApJ, 524, 169
Mac Low, M. -M., & Klessen, R. 2004, RvMP, 76, 125
Mac Low, M. -M., Klessen, R., Burkert, A., & Smith, M. D. 1998, Phys. Rev. Lett., 80, 2754
Margulis, M., Lada, C. J., & Snell, R. L. 1988, ApJ, 333, 316
Matzner, C. D. 2007, ApJ, 659, 1394
Matzner, C. D., & McKee, C. F. 2000, ApJ, 545, 364
Meyer, M. R., Adams, F. C., Hillenbrand, L. A., Carpenter, J. M., & Larson, R. B. 2000, in Protostars and Planets IV, ed. V. Mannings et al., 521
Motte, F., & André, P. 2001, A&A, 365, 440
Motte, F., André, P., & Neri, R. 1998, A&A, 336, 150
Motte, F., André, P., Ward-Thompson, D., & Bontemps, S. 2001, A&A, 372, 41
Myers, P. C. 2000, ApJ, 530, 119
Nakamura, F., & Li, Z. -Y. 2007, ApJ, 662, 395
Norman, C., & Silk, J. 1980, ApJ, 238, 158
Padoan, P., & Nordlund, A. 2002, ApJ, 576, 870
Palla, F., & Stahler, S. 1999, ApJ, 525, 772
Peretto, N., André, Ph., & Belloche, A. 2006, A&A, 445, 979
Peretto, N., Hennebelle, P., & André, Ph. 2007, A&A, 464, 983
Quillen, A., Thorndike, S., Cunningham, A., et al. 2005, ApJ, 632, 941
Reipurth, B., & Bally, J. 2001, ARA&A, 39, 403
Robitaille, T., Whitney, B., Indebetouw, R., & Wood, K. 2007, ApJ, 169, 328
Rodriguez, L. F., Canto, J., Torrelles, J. M., & Ho, P. T. P. 1986, ApJ, 301, 25
Rodriguez, L. F., Porras, A., Claussen, M. J., et al. 2003, ApJ, 586, 137
Schreyer, K., Helmich, F. P., van Dishoeck, E. F., & Henning, T. 1997, A&A, 326, 347
Schreyer, K., Stecklum, B., Linz, H., & Henning, Th. 2003, ApJ, 599, 335
Schuster, K.-F., Boucher, C., Brunswig, W., et al. 2004, A&A, 423, 1171
Scoville, N. Z., Sargent, A. I., Sanders, D. B., et al. 1986, ApJ, 303, 416
Shu, F. H., Li, Z.-Y., & Allen, A. 2004, ASPC, 323, 37
Snell, R. L., Loren, R. B., & Plambeck, R. L. 1980, ApJ, 239, 17
Solomon, P. M., Rivolo, A. R., Barrett, J., & Yahil, A. 1987, ApJ, 319, 730
Stahler, S. W. 1988, ApJ, 332, 804
Stanke, T., Smith, M. D., Gredel, R., & Khanzadyan, T. 2006, A&A, 447, 609
Stojimirović, I., Narayanan, G., Snell, R. L., & Bally, J. 2006, ApJ, 649, 280
Strom, S. E., Strom, K. M., Grasdalen, G. L., et al. 1984, BAAS, 16, 465
Talvard, M., André, Ph., Rodriguez, L., et al. 2008, SPIE, 7020, 70200
Taylor, D. K., & Dickman, R. L. 1989, ApJ, 341, 293
Testi, L., & Sargent, A. 1998, ApJ, 508, 91
Umemoto, T., Iwata, T., Fukui, Y., et al. 1992, ApJ, 392, 83
Von Weizsäcker, C. F. 1951, in Proceedings of a Symposium on the Motion of Gaseous Masses of Cosmical Dimensions, 1949, 158
Wang, H., Yang, J., Wang, M., & Yan, J. 2002, A&A, 389, 1015
Ward-Thompson, D., Zylka, R., Mezger, P. G., & Sievers, A. W. 2000, A&A, 355, 1122
Williams, J., & Garland, C. 2002, ApJ, 568, 259
Wilson, T. L., & Matteucci, F. 1992, A&A, 4, 1
Wolf-Chase, G. A., Walker, C. K., & Lada, C. J. 1995, ApJ, 442, 197
Wolf-Chase, G. A., & Walker, C. K. 1995, ApJ, 447, 244